國立臺灣大學理學院物理學系

博士論文

Department of Physics

College of Science

National Taiwan University

Doctor Thesis

低維度二六族半導體核殼奈米線之成長與特性分析

Growth and Characterization of Low-dimensional

II-VI Semiconductor Core-shell Nanowires

趙軒逸

Hsuan-Yi Chao

指導教授：張顏暉 博士

Advisor: Yuan-Huei Chang, Ph.D.

中華民國99年1月

January, 2010

誌 謝

轉眼間，在台大的碩、博士班生涯結束了，人生將邁入另一個嶄新的里程。

多年來最感謝的人就是我們所敬愛的張顏暉老師，張老師樂觀積極的教學、實事

求是的做事態度，以及對物理實驗的感覺和觀點，使我在實驗研究方面獲益良

多。也非常感謝張老師對我的關心與照顧，讓我在實驗受挫時感到無比的溫暖。

另外也很感謝陳永芳老師和梁啟德老師在我每次報告及畢業口試時，都能給予寶

貴的意見和正確地指出問題的所在。此外也很感謝口試委員中興大學物理系孫允

武教授和海洋光電所所長林泰源教授，在畢業口試及論文上給予極寶貴的意見，

使得這本論文更加地完整。

從進來台大到畢業這期間要感謝的人真是太多人，從學長、學姊到學弟、學

妹等都是我的貴人。感謝大家在實驗上的幫助及意見，使我學習到不少知識及技

術。最感謝的就是實驗室的老大哥日新及景翔學長，從碩班一路帶領我到博班，

不論是機台維修、實驗測量及研究討論都給予我極大的幫助、意見和方向，使我

在實驗上有所成就。多年來照顧我如親兄弟，大家感情有如手足之情，不論到哪

裡都是一起行動的。駿佑的加入使我在實驗上獲得許多幫助及寶貴的建議，謝謝

你時時幫我加油、打氣。義大利的照片我會常拿出來看的。聖涵、辛宇、俊昌、

小戴，感謝你們在實驗上的支援與幫忙，讓我可以如期畢業！還有仲良學長、志

瑋、群雄、函宇、鴻齊…等，謝謝你們的幫助才使這本論文更加豐富。感謝我從

小到大的朋友們及表哥日昌、日新，謝謝你們的鼓勵讓我有動力繼續奮鬥下去。

I

最後我要感謝我的父母，從小對我的栽培與細心照顧。感謝媽媽每天從早到晚幫忙照顧爸爸，讓我可以放心在學校做實驗。感謝大姊、二姊分擔家計，讓我可以無後顧之憂完成博士學位。爸爸、媽媽，我做到了！
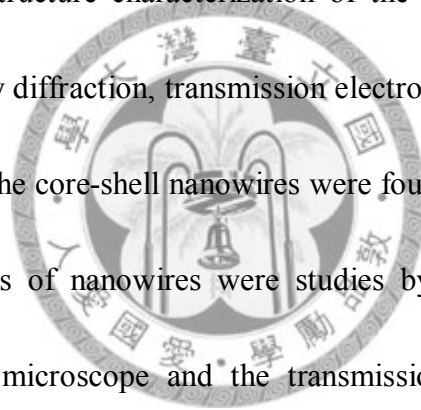
摘要

　　由於在製作電子和光電元件應用方面有很大的潛力，最近低維度半導體例如

奈米線、奈米柱和奈米管已經吸引很多人的注意。在此論文中，我們報告有關於

II-VI 族奈米線的成長及特性分析和光電性質。在 ZnO 奈米線和 ZnO/ZnTe 核殼

奈米線的研究方面，我們使用化學氣相沉積法和有機金屬化學氣相沉積法，成功

地製作出 ZnO/ZnTe 核殼奈米線結構。我們使用多種結構分析儀器也確認樣品具

有良好結晶結構。在光學儀器分析下，結果也顯示樣品是具有好的光學性質。然

後我們取單根 ZnO/ZnTe 核殼奈米線製作成單根的電晶體，研究它的電學特性，

結果顯示出施加的電壓可以控制它的電流大小。除了在 ZnO/ZnTe 系統中，我們

也成功地成長出 ZnO/ZnSe 核殼奈米線。這 ZnO/ZnSe 核殼奈米線也是具有好的結

晶結構和光學性質。

Abstract

Because of their potential applications in making electronic and opto-electronic devices, low-dimensional semiconductor systems such as nanowires, nanorods and nanotubes have attracted great attention recently. In this thesis we report our studies on the growth and characterization of II-VI semiconductor nanowires and the opto-electronic properties of these nanowires. ZnO/ZnTe core-shell nanowires were successfully fabricated by first growing the ZnO core then ZnTe shell by CVD and MOCVD, respectively. Structure characterization of the core-shell nanowires were carried out by using X-ray diffraction, transmission electron microscope and scanning electron microscope and the core-shell nanowires were found to have good crystalline quality. Optical properties of nanowires were studies by using Raman scattering, confocal laser scanning microscope and the transmission measurements and the results also indicate the nanowires have good optical properties. The nanowire is then made into a single nanowire transistor and its electric properties were studied and the result indicates that it has proper biasing properties and can be use as a functional transistor. In addition to the ZnO/ZnTe system, the ZnO/ZnSe core-shell nanowires were also grown successfully by using the same growth methods. The ZnO/ZnSe nanowires were also found to have good crystal structure and optical properties.

Contents

Chapter 3   Sample preparation

Chapter 4   Growth and characterization of type-II ZnO/ZnTe core-shell nanowire arrays

List of Figures

Chapter 1

Introduction

1.1 Growth and characterization of type-II ZnO/ZnTe core-shell nanowire array

Type-II semiconductor heterojunction solar cells have attracted much attention recently because the type-II band alignment of these heterostructures separates the electron and hole in different regions of the samples naturally and is thus are ideal candidates for making solar cell. Although there are many reports on the investigation of organic/inorganic heterostructure for making solar cell such as combining CdSe nanorods with poly (3-hexylthiophene) (P3HT) [1, 2] and combining CdTe nanorods with polymer (P3OT) [3]. However, there are very few reports on the synthesis of all semiconductor core-shell nanowires with type-II band alignment for solar cell application [4]. J. Schrier *et al*. [5] studied theoretically the optical properties of ZnO/ZnS and ZnO/ZnTe heterostructures and they found that the ZnO/ZnS core-shell nanowire structure has wider absorption spectrum than that of ZnO/ZnS planar structure as shown in figure 1.1.1. They also concluded that the theoretical limit of ideal solar cell efficiency was 30 ％ for ZnO/ZnTe heterostructures, which is higher than that of ZnO/ZnS structure. The results indicated that the ZnO/ZnTe structure has
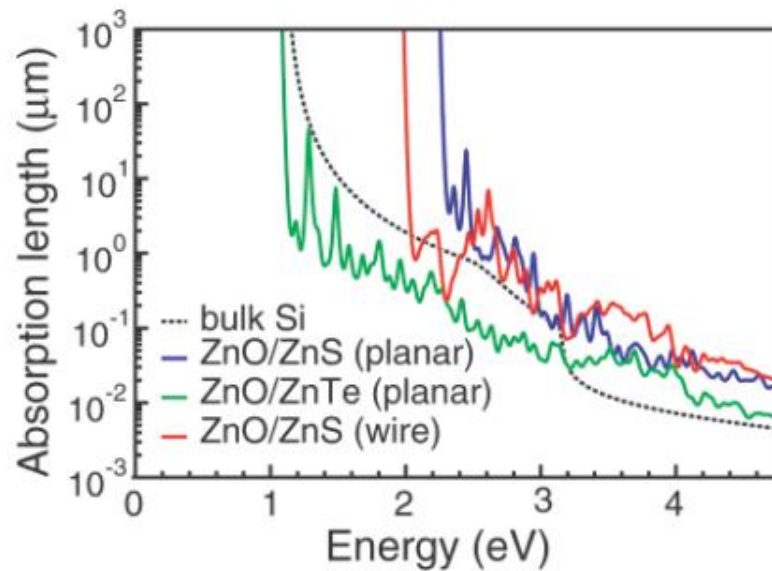
Fig 1.1.1 Absorption length as a function of the energy of the incident light for

various semiconductor structures. The blue and green lines are the values

calculated for the ZnO/ZnS and ZnO/ZnTe planar heterostructures as

discussed in Section IIIA; the red line is the value calculated for the

ZnO/ZnS core/shell nanowire discussed in Section IIIB. The dotted black

line shows the experimental data for bulk Si at 300 K. (Joshua Schrier et al.

Nano Lett. **7**, 2377-2382 (2007))

great potential application in making photovoltaic devices.

In this study, we report the growth and characterization of large area, well-aligned type-II ZnO/ZnTe core-shell nanowire arrays. The morphology and size distribution of the ZnO/ZnTe core-shell nanowire arrays were studied by scanning electron microscopy and it was found that the surfaces of the well-aligned ZnO nanowires became rougher after the growth of ZnTe layer and the diameter of the nanowire increase from 70-100 nm to 150-300 nm. X-ray diffraction and transmission electric microscopy show that the ZnO core has wurtzite structure, the ZnTe shell has zinc-blende structure and both materials have good crystalline quality.
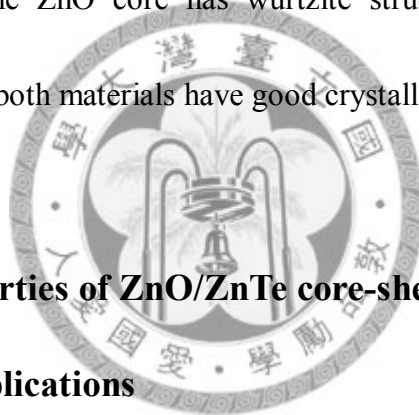
1.2 The optical properties of ZnO/ZnTe core-shell nanowire and its device applications

In addition to making photovoltaic devices ,one-dimensional ZnO nanowires have also attracted a great deal of attention for their potential applications in making electronic, opto-eletronic and sensor devices such as ultra-violet photodetectors [6, 7], chemical sensors [8], biological sensors [9] and UV laser [10]. Because the nanowires have large surface to volume ratio, the surface effect, especially the effect of surface defects on the performance of ZnO-nanowire-based device can not be overlooked. For example, it is known that oxygen chemisorption plays a central role in regulating the

photosensitivity of ZnO [11, 12]. Oxygen molecules adsorbed on the nanowire surface behaved as negatively charged ions by capturing free electrons from ZnO, thereby creating a depletion layer with low conductivity near the surface as shown in figure 1.2.1 [13]. In addition, the effects of both oxygen and water molecules adsorbed on ZnO nanowires on the UV photoresponse of ZnO nanowires have also been studied. The band alignments of the ZnO nanowires in the presence of oxygen and water molecules are depicted in figure1.2.2 [14]. In order to improve the stability of the performance of the ZnO-nanowire-based devices, it is desirable to passivate the surface of the ZnO nanowire. In this study, we report the growth and characterization of ZnO/ZnTe core-shell nanowires and their electrical and optical properties. In this structure the ZnTe layer not only serves the purpose of passivating the ZnO surface; it also forms a type-II semiconductor heterosructure with the ZnO core layer. Raman scattering and laser scanning confocal microscopy is used for analyzing optical characterization of nanostructures. In Raman spectrum the A_1 (LO) made of ZnO at 574 cm^{-1}, the LO mode of ZnTe at 412 cm^{-1} and the TO mode of ZnTe at 206 cm^{-1} indicate that the core cell structure have high-quality crystalline quality. The three dimension photoluminescence image indicates that the light emission along nanowire is quite uniform. The nanowire is then made into a single nanowire transistor and its electric properties were studied and the result indicates that it has proper biasing
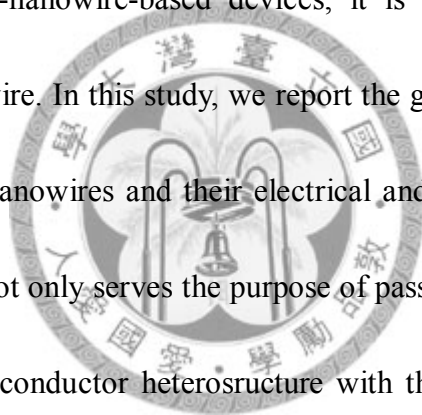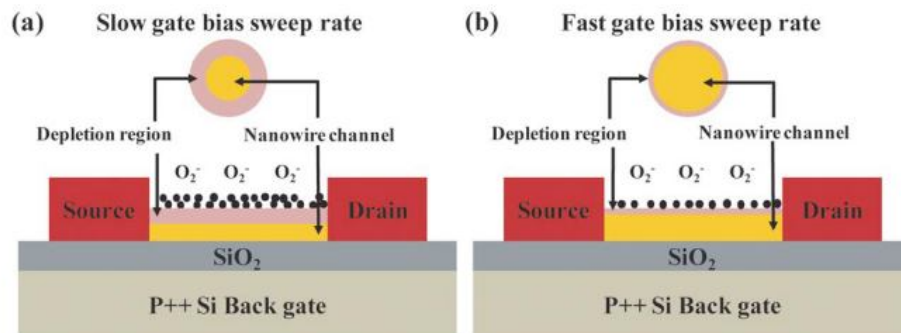
Fig 1.2.1 Schematic diagram illustrating the effect of gate bias sweep rate in a

ZnO nanowire field effect transistor. A larger depletion region is formed

with slower gate bias sweep rates (a) than the case for faster gate bias

sweep rate (b). (J. Maeng *et al.* , Appl. Phys. Lett. **92**, 233120 (2008))
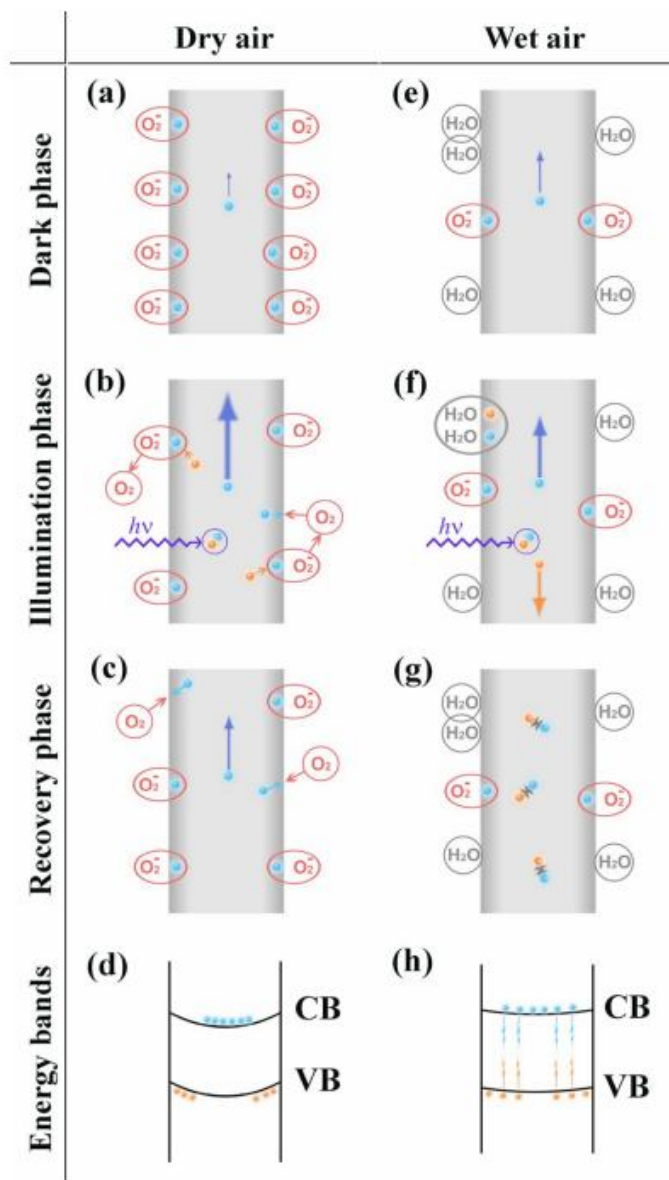
Fig. 1.2.2 Schematic diagrams of the valence band and the conduction band of a ZnO nanowire in [(a)-(d)] dry air, and [(e)-(f)] wet air. Blue and orange dots represent electrons and holes, respectively. (Y. Li *et al*. , Appl. Phys. Lett. **94**, 023110 (2009))

properties and can be use as a functional transistor.

1.3 Growth and characterization of ZnO/ZnSe core-shell nanowires

Vertically aligned, large area ZnO/ZnSe core-shell nanowires were synthesized by using chemical vapor deposition and metal-organic chemical vapor deposition techniques. The samples were than studied X-ray diffraction, Raman scattering, and laser scanning confocal microscopy. The results show the ZnO nanowire has wurtzite structure along the [002] direction and the ZnSe shell has zinc-blende structure. Bothe the ZnO and ZnSe phonon modes can be observed in Raman spectrum, it indicates that the sample is a core-shell structure and the strain is fully relaxed at the interface. Three-dimensional photoluminescence image indicates that the light emission along nanowire is quite uniform. The results demonstrate that ZnO/ZnSe core-shell nanowires have both good structural and optical properties.
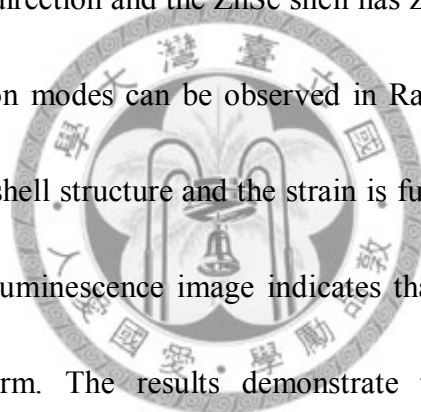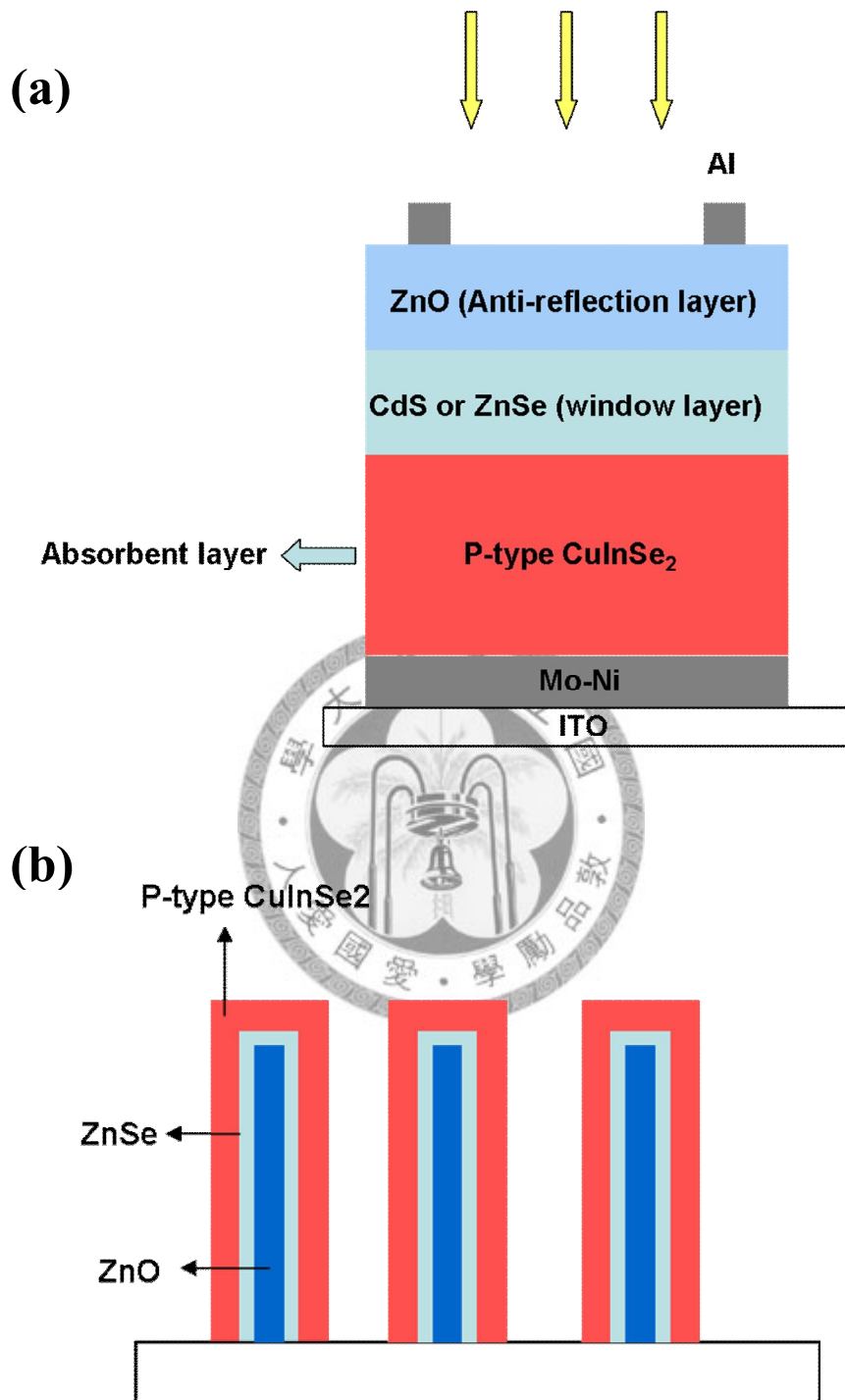
Fig 1.3.1 (a) Illustration of a CuInSe$_2$ solar cell, and (b) Illustration of a

ZnO/ZnSe/CuInSe$_2$ nanowires solar cell structure.

References

[1] W. U. Huynh, J. J. Dittmer, and A. P. Alivisatos, Science. **295**, 2425 (2002).

[2] W. U. Huynh, J. J. Dittmer, W. C. Libby, G. L. Whiting, and A. P. Alivisatos, Adv. Funct. Mater. **13**, 73 (2003).

[3] Y. Kang, N. G. Park, and D. Kim, Appl Phys.Lett. **86**, 113101 (2005).

[4] Wang, K., Chen, J., Zhou, W., Zhang, Y., Yan, Y., Pern, J., and Mascarenhas, A., Adv. Mater **20**, 3248 (2008).

[5] J. Schrier, D. O. Demchenko, and L.-W. Wang, Nano Lett. **7**, 2377 (2007).

[6] W. I. Park, Y. H. Jjun, S. W. Jung and G. C. Yi, Appl. Phys. Lett. **82**, 964 (2003).

[7] L. B. K. Law and J. T. L Thong, Appl. Phys. Lett. **88**, 133114 (2006).

[8] Q. Wan, Q. H. Li, Y. J. Chen, T. H. Wang, X. L. He, J. P. Li and C. L. Lin, Appl. Phys. Lett. **84**, 3654 (2004).

[9] H. T. Wang, B. S. Kang, F. Ren, L. C. Tien, P. W. Sadik, D. P. Norton, S. J. Pearton and J. Lin, Appl. Phys. Lett. **86**, 243503 (2005).

[10] R. Q. Guo, J. Nishimura, M. Matsumoto, M. Higashihata, D. Nakamura, J. Suehiro and T. Okada, Appl. Phys. B **90**, 539 (2008).

[11] Y. Lin, D. Wang, Q. Zhao, Z. Li, Y. Ma and M. Yang, Nanotechnology **17,** 2110 (2006).

[12] J. D. Prades, F. Hernandez-Ramirez, R. Jimenez-Diaz, M. Manzanares, T. Andre,

A. Cirera, A. Romano-Rodriguez and J. R. Morante, Nanotechnology **19**, 465501 (2008).

[13] J. Maeng, G. Jo, S.-S. Kwon, S. Song, J. Seo, S.-J. Kang, D.-Y. Kim, and T. Lee. Appl. Phys. Lett. **92**, 233120 (2008).

[14] Y. Li, F. D. Valle, M. Simonnet, I. Yamada, and J.-J. Delaunay. Appl. Phys. Lett. **94**, 023110 (2009).
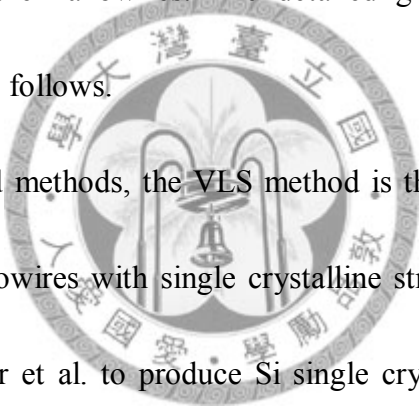
Chapter 2

Growth methods and measurement techniques

2.1 The growth of ZnO nanowires

Many different methods can be used to grow ZnO nanowires and nanorods. Vapor-phase transport via a vapor–liquid–solid (VLS) mechanism [1, 2], vapor solid mechanism [3, 4], gas reaction [5], and oxidation of metal in the pores of anodic alumina templates [6] are just few examples. In this thesis, the vapor-phase transport was used to synthesize the nanowires. The detailed growth mechanisms of the nanowires are discussed as follows.

Among the vapor based methods, the VLS method is the most successful one for fabricating large area nanowires with single crystalline structures. This process was first developed by Wagner et al. to produce Si single crystalline micro-whiskers in 1960s [7], and recently rediscovered and used successfully by Lieber [8] and Yang [3, 4]. The critical step of the VLS growth is to deposit metal particles such as Pt, Ag, Cu, and Au as the catalysts. A typical VLS process starts with the dissolution of gaseous reactants into liquid droplets of catalyst metal when the liquid droplets are supersaturated with the reactant materials, followed by nucleation and growth of single crystalline nanowires. The 1D growth is mainly induced and dictated by the liquid droplets, whose size remains essentially unchanged during the entire process of

11

nanowire growth. On the other hand, each of liquid droplets serves as a template to restrict the lateral growth of an individual nanowire. A major requirement for VLS process is that there should be a good solvent capable of forming liquid alloy with the reactant materials [9] and they should be able to form a low melting point eutectic alloy. The major steps involved in a VLS process are schematically illustrated in figure 2.1.1 Reactant materials and metal catalysts form liquid alloy when the temperature is raised above the eutectic point. The growth of nanowire begins after the liquid becomes supersaturated in reactant materials and continues as long as the reactant materials are available and the catalyst alloy remains in a liquid state.
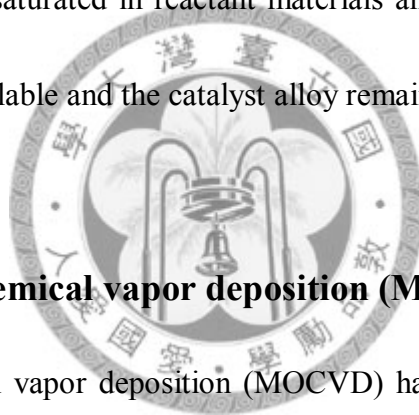
2.2 Metal-organic chemical vapor deposition (MOCVD)

Metal-organic chemical vapor deposition (MOCVD) has become one of the most widely used techniques for the growth of advanced semiconductors thin films, quantum well, quantum dots and devices at the commercial scale. The technology also has now established its ability to produce high-quality epitaxial layers with sharp interfaces and to grow multilayer structures with thickness as thin as a few atomic layers. The MOCVD growth process is based on the pyrolysis of alkyls or metal-organics in an atmosphere of hydrides. The controlled amounts of volatile compounds of alkyls and hydride gases are introduced into a reaction chamber in
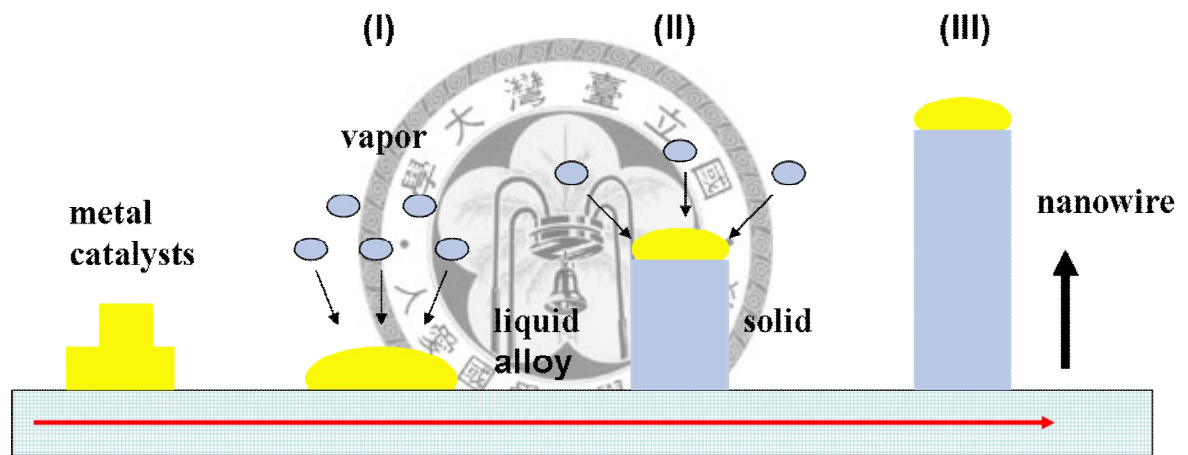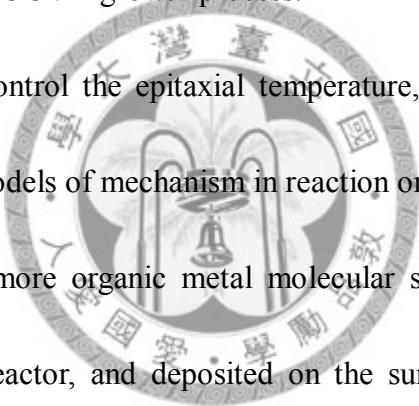
Fig. 2.1.1 (a) Schematic illustration of vapor-liquid-solid growth mechanism, which

includes three stages, (I) alloying, (II) nucleation and (III) axial growth.

which a substrate is placed on a heated holder. The latter has a catalytic effect on the decomposition of the gaseous products, such that the semiconductor crystal growth takes place in this hot region. The schematic diagram of an MOCVD reactor is shown in figure 2.2.1, which depicts the gas handling system and the reactor chamber.

The gas handling system includes the alkyl and hydride sources and the valves, pumps, and other instruments necessary to control the gas flow and mixtures. Hydrogen (H_2), nitrogen (N_2), argon (Ar), and helium (He) are the common inert carrier gases used in the MOCVD growth process.

Therefore, we can control the epitaxial temperature, pressure and the flow of reactant. There are four models of mechanism in reaction on the surface:

(1) Phsisoption: Two or more organic metal molecular sources are transported by carrier gases to the reactor, and deposited on the surface of substrate. This is so-called gaseous phase deposition.

(2) Chemisoption: After organic metal deposition, heating makes the bonds between metal and organic molecules broken. Thereafter, metals are bound together due to chemical reaction, and organic molecules dissociated with metal. The organic molecules with carrier gases are drawn away by pump.

(3) Diffusion: The semiconductor molecules are still grown slowly on the reacting surface.
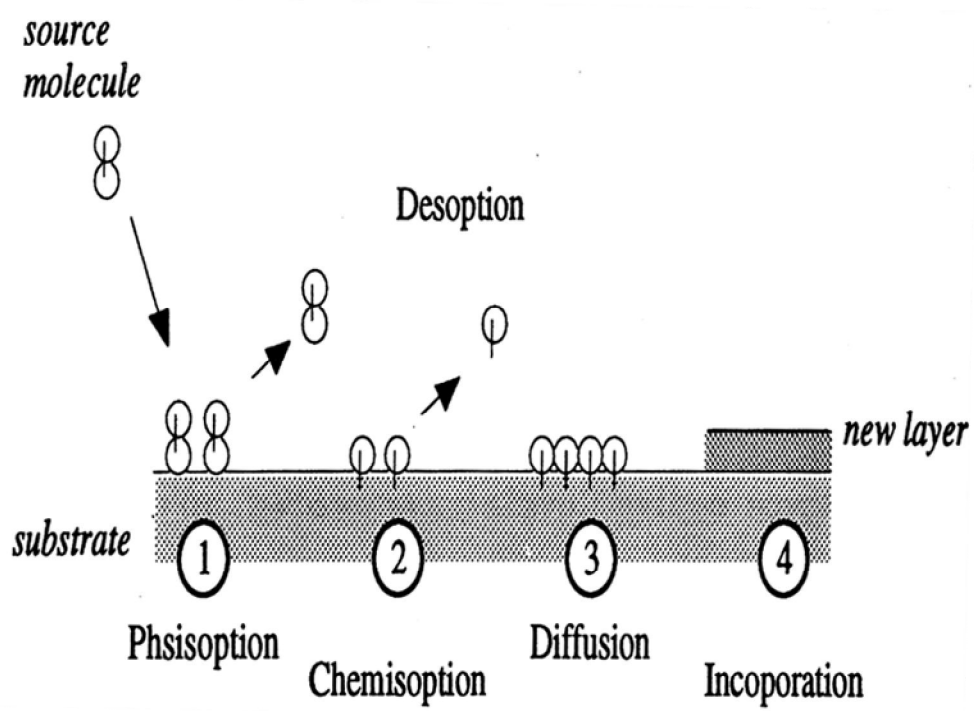
Fig. 2.2.1 Reaction regimes on the substrate surface.

(4) Incorporation: The epilayer is formed on the substrate. The thickness of the epilayer is determined by the duration of the epitaxial process. The lattice mismatch between epilayer and substrate would produce a strain, so two dimensional layer formation is not maintain steadily and it is replaced by three dimensional island formation when the thickness of the epilayer is over a critical thickness.

When the process is a heteroepitaxial growth, especially growing thin film or quantum well structures, the growth mode is very important and there are three well-known heteroepitaxial growths: Frank-Van der Merwe mode (FvdM), Volmer-Weber mode (V-W) and Stranski-Krastanow mode (S-K). They represent layer-by-layer growth (FvdM, 2D), island growth (V-W, 3D), and layer-by-layer plus island (S-K), respectively (see figure 2.2.2). The particular growth mode for a given system depends on the interface energies and on the lattice mismatch.

In lattice-matched systems, the growth mode is solely governed by the interface and surface energies. If the sum of the epilayer surface energy γ_2 and of the interface energy γ_{12} is lower than the energy of the substrate surface γ_1 ($\gamma_2+\gamma_{12}<\gamma_1$), the FvdM mode occurs. A change in $\gamma_2+\gamma_{12}$ alone may drive a transition from the FvdM to the V-W growth mode. For a strained epilayer with small interface energy, initial growth may occur layer by layer, but a thicker layer has large stain energy and can lower its
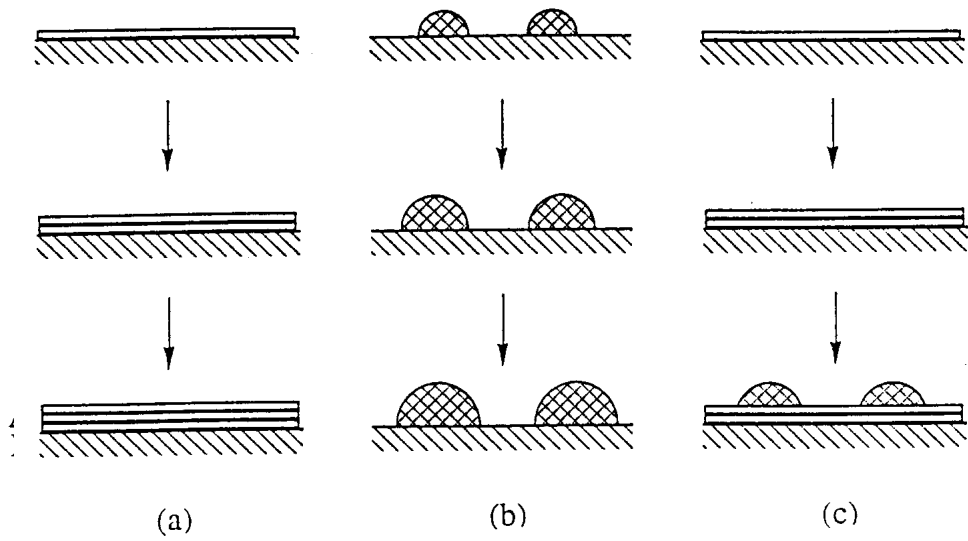
Fig. 2.2.2 Schematic diagram of various growth modes: (a) Frank-van der Merwe, (b)

Volmer-Weber, and (c) Stranski-Krastanov.
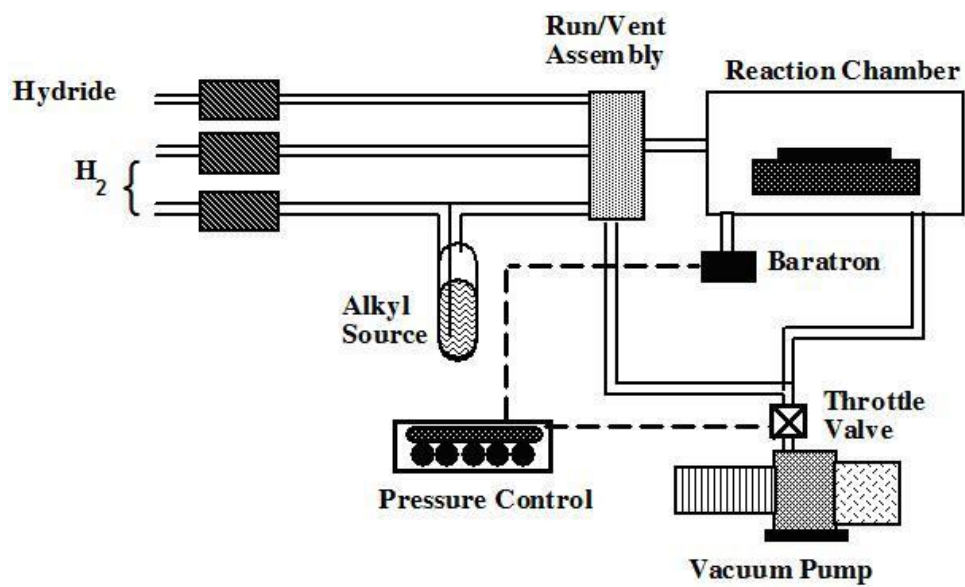
Fig. 2.2.3 Schematic diagram of MOCVD system. (G. B. Stringfellow. Organometallic

Vapor-Phase Epitaxy：Theory and Practice, 2nd ed. Academic Press (1999)).

energy by forming isolated islands in which strain is relaxed. Thus the S-K growth mode occurs.

The MOCVD system is shown in figure 2.2.3 [10], which includes reactor chamber, gas handling and mixing system, precursor and scrubber.

2.3 Photoluminescence (PL)

An optical excitation with photon energy exceeds the bandgap of the semiconductor to be examined incident on the semiconductor will cause the semiconductor to emit a specific spectrum, which is optical characterizations of the sample and the process is called photoluminescence. The details of PL include the following processes: when electrons in valence band absorb the energy from laser beam, they are excited to conduction band and leave vacancies (holes) in valence band. Electrons and holes arrive at the bottom of conduction band and the top of valence band respectively through rapid relaxation. The emission of photons in luminescence processes is due to an electronic transition between an initial state E_i and the final state E_f. The energy of the emitted photon can be found from the relation $h\nu = E_f - E_i$. From the peak position and line-width in the spectrum obtained from PL experiment, the bandgap and quality of the material can be obtained [11]. In addition, many kinds of recombination could occur as were shown in figure 2.3.1. The intensity

and peak position of the PL emission depends on optical qualities of a sample.

2.4 Scanning electron microscopy (SEM)

The basic components of a SEM are lens system, electron gun, electron collector, and visual system [12]. Figure 2.4.1 shows the schematic of a scanning electron microscope, containing the secondary electron detector. Energetic electrons are injected into the system as an electron gun.

In a SEM system, a source of electrons is focused into a beam, with a fine spot size of ~5 nm and having energy ranging from about 1 keV to 50 keV. As the electrons strike and penetrate the surface, a number of interactions occur that result in the emission of electrons and photons from the sample. Various SEM techniques are differentiated on the basis of what is subsequently detected and imaged, and the principle images produced in the SEM are of several types, such as the secondary electron images, backscattered electron images and elemental X-ray maps [13, 14]. When the electron interacts with an atom, it undergoes either inelastic scattering with atomic electrons or elastic scattering with the atomic nucleus. In an inelastic collision with an electron, the primary electron transfers part of its energy to the loosely-bound conduction band electrons in the sample.

When the energy transfer is large enough, the conduction band electron will emit
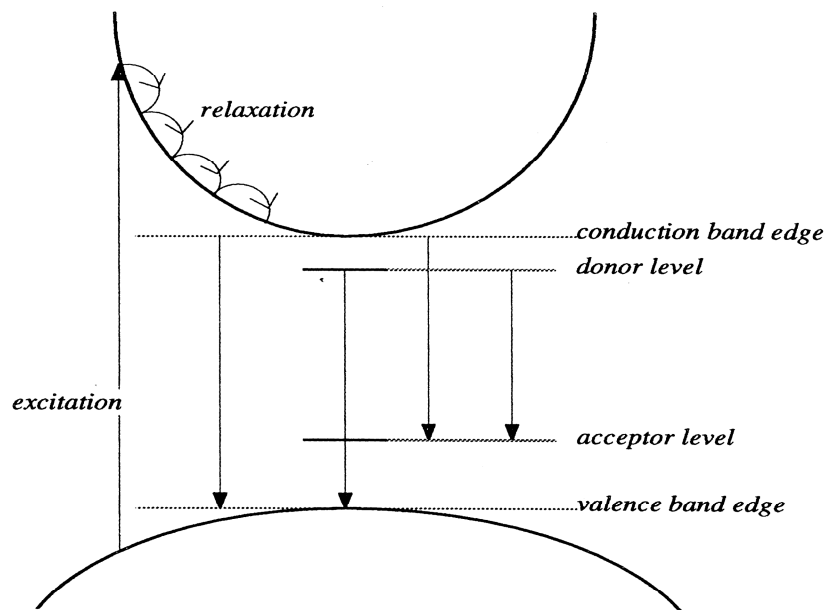
Fig. 2.3.1 Schematic diagram of the mechanisms for the photoluminescence.
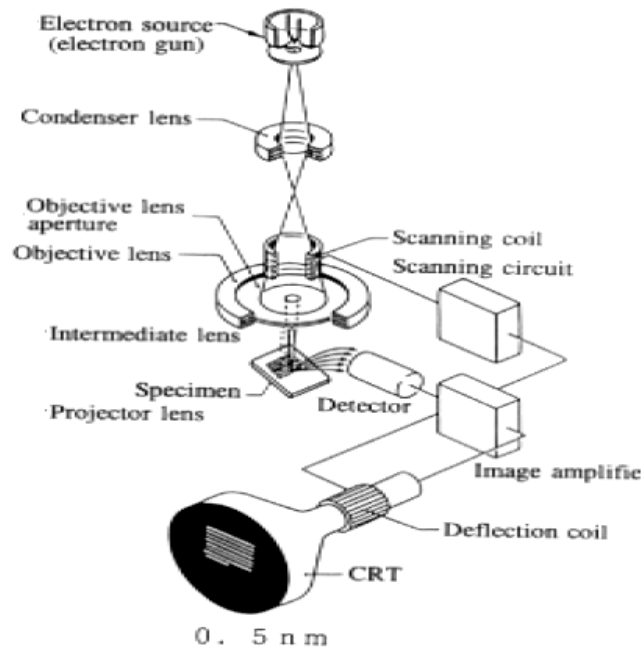
Fig. 2.4.1 Basic components of the SEM system. (G. I. Goldstein, D. E. Newbury, P.

Echlin, D. C. Joy, C. Fiori, and E. Lifshin, Scanning electron microscopy

and X-ray microanalysis, Plenum Press, New York and London (1981)).

from the sample, which calls secondary electrons. The secondary electrons are emitted

from the atoms occupying the top surface layer and produce an image of the surface.

The amount of energy given to these secondary electrons as a result of the interactions

is small, and so they have a very limited range in the sample (a few nm). Because of

this, only those secondary electrons that are produced within a very short distance of

the surface are able to escape from the sample. This means that this detection mode

boasts high resolution topographical images, making this the most widely used of the

SEM modes.

Backscattered electrons are primary beam electrons, which are reflected by the

atoms in the surface layers. The contrast in the image produced is determined by the

atomic number of the elements in the surface layers. Therefore, the image will show

the distribution of different chemical phases in the specimen surface. Because

backscattered electrons are emitted from a depth in the specimen, the resolution in the

image is usually not as good as for secondary electrons. The probability of

backscattering increases with the atomic number of the sample material. Although

backscattering images can not be used for elemental identification, useful contrast can

develop between regions of the specimen that differ widely in atomic number.

When the primary electron collides with a sample and ejects a core electron from

an atom, the excited atom will decay to its ground state by emitting a characteristic
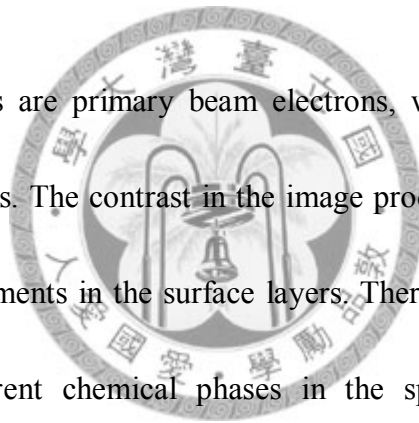
X-ray photon, and the emitted X-ray has an energy that is characteristic of its parent element. Thus detection and measurement of X-ray energy permits elemental analysis and is commonly referred to as Energy Dispersive X-ray Spectroscopy (EDS). EDS can provide rapid qualitative, or with adequate calibration standards, quantitative analysis of elemental composition in a depth of 1~2 micro meters for a sample. X-rays may also be used to form maps or line profiles, showing the elemental distribution in a specimen surface. Combining with chemical analytical capabilities, SEM not only can provide the image of the morphology of nanostructure materials but also can confirm detailed information of chemical compositions and distributions.

The depth of electron penetration is the electron range r_e, defined as the average total distance from the sample surface that and electron travels in the sample along a trajectory. A number of empirical expressions have been derived for r_e. One such expression is

$$r_e = \frac{4.28 \times 10^{-6} E^{1.75}}{\rho} (cm),$$ (2.4-1)

where ρ is the sample density (g/cm^3) and E the electron energy (KeV). Besides, the theoretical limit to an instrument's resolving power is determined by the wavelengths of the electron beam used and the numerical aperture of the system. The resolving power of an instrument is defined as:

$$R = \frac{\lambda}{2NA},$$ (2.4-2)

Where R is resolution, λ is the wavelength of incident electrons, and *NA* is the numerical aperture. The resolution is engraved on each objective and condenser lens system, including a measure of the electron gathering ability of the objective and the electron providing ability of the condenser.

In the SEM setup, the focused electron beam is scanned over a sample surface at the same time as the acquired signal is projected on to a CRT or into an image memory. Figure 2.4.1 shows the basic components of the SEM system. The scanning electron microscopy generates a beam of electrons under high vacuum at the top of the microscope by heating a metallic element. That beam is collimated by electromagnetic condenser lenses, focused by an objective lens and scanned across the surface of the sample by electromagnetic deflection coils. The magnetic condenser and objective lens system shown in figure 2.4.1 serve to reduce the image at the crossover (10 to 50 μm) to a final spot on the sample of 5 to 200 nm. The condenser lens system, which may consist of one or more lenses, is responsible for the throughput of the electron beam reaching the objective lens; the objective lens is responsible for the size of the electron beam impinging on the surface of the sample. Typically, an individual lens is cylindrically symmetrical and between 10 an 15 cm in height. The primary imaging method is by collecting secondary electrons that are released by the sample. The secondary electrons are detected by a scintillation
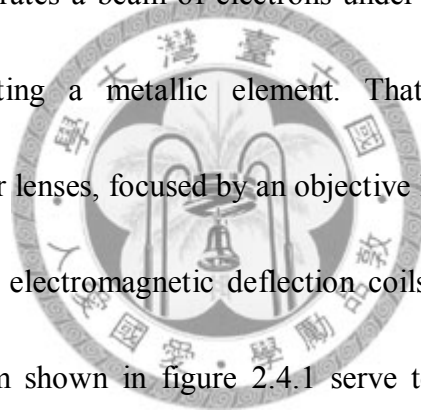
material that produces flashes of light from the electrons. The light flashes are then

detected and amplified by a photomultiplier tube. By correlating the sample scan

position with the resulting signal, an image can be formed that is strikingly similar to

what would be seen through an optical microscope, which shows a quite natural

looking surface topography.

2.5 X-ray diffraction (XRD)

X-ray diffraction is a nondestructive technique for analyzing sample crystal

properties, and it also can identify crystalline phases and orientation. Moreover, X-ray

powder method is based upon the fact that an X-ray diffraction pattern is unique for

each crystalline material. Thus the pattern of an unknown structure can be contrasted

with the database of these crystalline powders, and then the structural identity can be

carried out. In a diffraction experiment, the X-rays are produced whenever high-speed

electrons collide with a metal target. A source of electrons-hot W filament, a high

accelerating voltage between the cathode (W) and the anode and a metal target, Cu, Al,

Mo, Mg. The anode is a water-cooled block of Cu containing desired target metal.

The wavelength of the incident X-ray must be similar to the spacing between atoms.

The incident X-ray is absorbed by the sample or transmits through it and only the

diffracted beam can be detected by the detector. The basic process is shown in
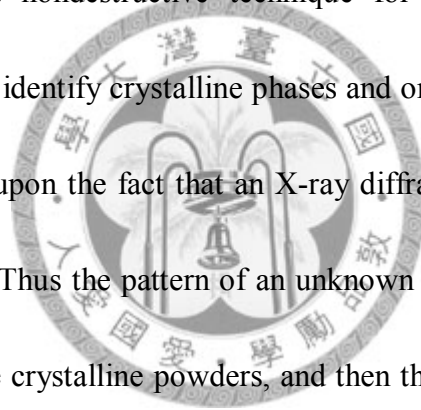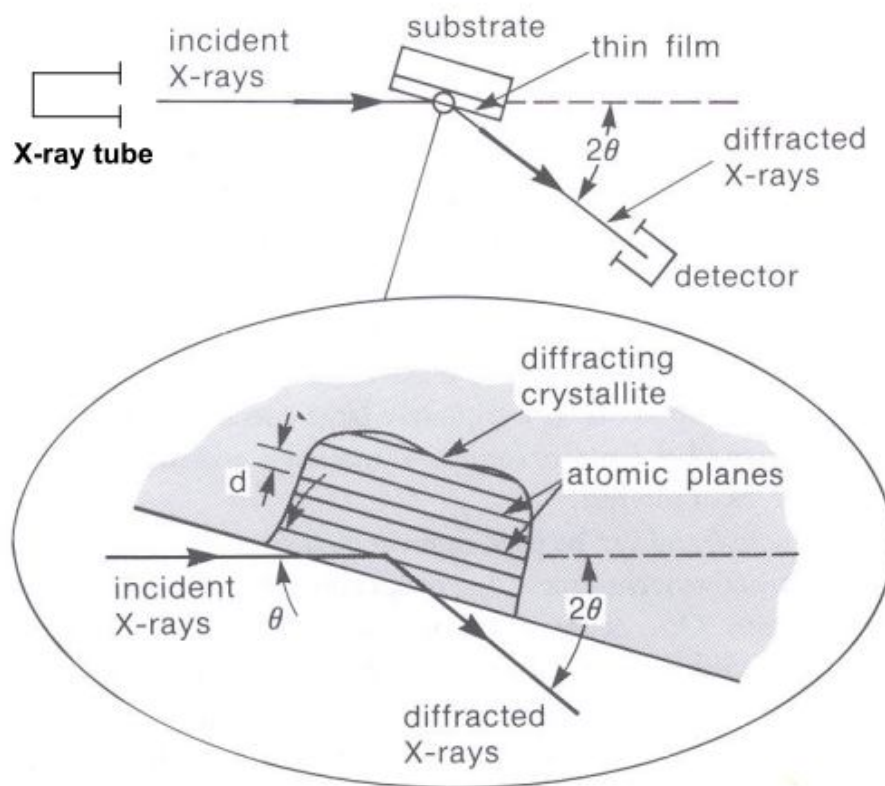
Fig. 2.5.1 Basic features of a typical XRD experiment
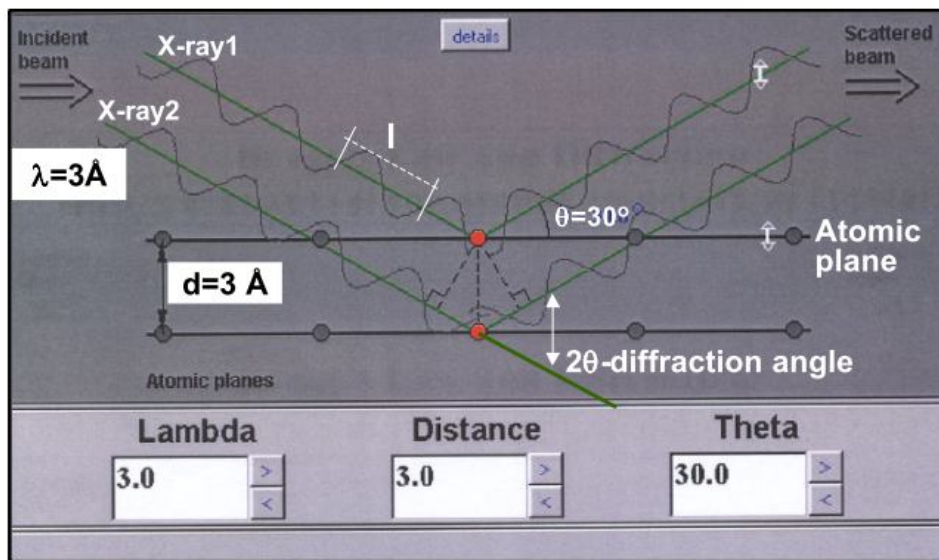
Fig. 2.5.2 Illustration of Bragg diffractions [15].

figure 2.5.1. Diffraction occurs only when Bragg's Law is satisfied the condition for

constructive interference (X-rays 1 & 2) from planes with spacing d.

Bragg's Law: $n \lambda = 2\, d_{hkl} \sin\theta$ (2.5-1)

Where d is the distance between atomic layers in a crystal, λ is the wavelength of the

incident X-ray beam; n is an integer and θ is measured from the plane as shown in

figure 2.5.2 [15]. In the diffraction experiment, we use a known λ and a measurement

θ to obtain values of d/n for the sample. The slow rotation of the sample about its axis

virtually ensures. In this experiment, XRD measurements are carried out using Cu Kα

(λ =0.1542 nm) radiation at 45 KV and 40 mA.

2.6 Confocal laser scanning microscope (CLSM)

Confocal measurement approach is widely used as important tools for measurement

of three-dimensional photoluminescence properties and surface contours because of

its good 3D chromatographic imaging capability. In addition, three-dimensional (3D)

mapping of the photoluminescence emission of single vertical nanowires was

performed using UV-laser scanning confocal microscopy. This unique method of

high-resolution microscopy combines a UV laser focused to a diffraction-limited spot

(~220 nm) with digital scanning electronics and a UV-enhanced detection system to

image the PL emission from planar sections of a ZnO vertical nanowire from base to

tip. The capability of this technique to selectively excite nanoscale regions of semiconductor nanowires in both horizontal and vertical geometries demonstrates a promising method for optically characterizing heterogeneous nanostructures for solar, LED, and optoelectronic applications.

The principle of a measurement system for a confocal microscopy [16, 17] is shown in figure 2.6.1. A laser light is used as excitation source, and the measuring lens is both the imaging lens and collecting lens in the setup. The laser is focused on a plane of a sample to excite the fluorescence by passing through a high resolution objective lens. However the reflective light from the defocal plane or the fluorescence excited from the sample can affect the photon excited from the focal plane, which makes the image not clear enough. The reflective light or the fluorescence from focus of the objective lens passes through these lenses to project on a small pinhole. In addition, the focus and the pinhole can be operated each other to detect a conjugate image which corresponds to the point light source from the sample. This is also why it is called confocal laser scanning microscope. The important advantage of the pinhole is that it can filter the most noise around the pinhole and make the detector collect the photons which reflect from the confocal plane. This characterization method could provide highly selective optical characterization of nanostructures emerging in the field of optoelectronics and nanophotonics that is unattainable by conventional
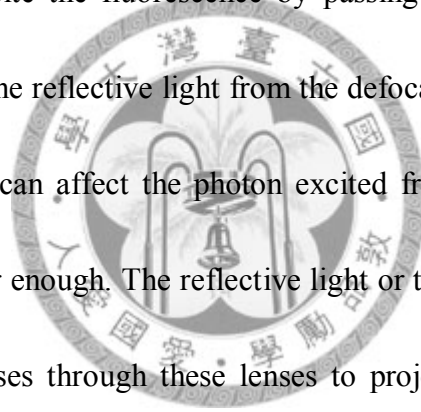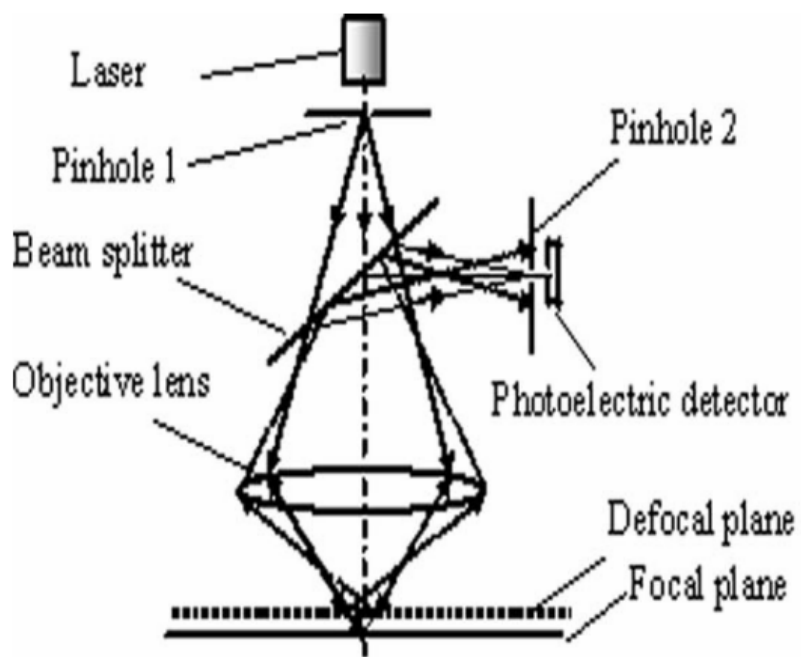
Fig. 2.6.1 Schematic diagram of a confocal microscopy system.

microscopy.

2.7 High-resolution transmission electron microscopy (HRTEM)

Direct imaging of nanostructures is only possible using TEM and scanning probe microscopy although some structural features can be revealed by X-ray and neutron diffraction. On the other hand, TEM is probably the most important and widely used characterization tool to study the nano-structrual characteristics of materials. In addition, TEM provides not only atomic-resolution lattice images but also chemical component at a spatial resolution of 1 nm or better.

The basic reason for utilizing the electron microscopy is its superior resolution, resulting from very small wavelengths as compared to other forms of radiation (light, X-rays, neutrons). The resolution is given by the Rayleigh formula, which is derived by considering the maximum angle of electron scattering, α, which can pass through the objective lens. This formula is

$$R=0.61\lambda/\alpha \qquad\qquad (2.7\text{-}1)$$

Where R is the size of the resolved object, λ is the wavelength, and α is identical to the effective aperture of the objective lens. Equation (2.7-1) is the classic Rayleigh criterion for resolution in light optics.

In a conventional TEM setup, a thin specimen is irradiated with an electron beam

of uniform current density; the electron energy is in the range 60-150 keV (usually

around 100 keV) or 200 keV-300 MeV in the case of intermediate or high-voltage

electron microscopy. Electrons are emitted in the electron gun by thermionic

emission from tungsten hairpin cathodes or LaB6 rods or by field emission from

pointed tungsten filaments. The letter is used when high gun brightness is needed. A

two-stage condenser-lens system permits variation of the illumination aperture and the

area of the specimen illuminated. The electron intensity distribution behind the

specimen is imaged with a three- or four-stage lens system, onto a fluorescent screen.

The image can be recorded by direct exposure of a photographic emulsion inside the

vacuum or digitally by CCD or TV cameras.
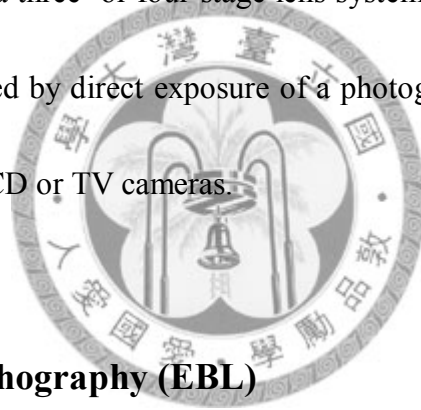
2.8 Electron beam lithography (EBL)

Electron beam lithography (EBL) is a lithographic process. In contrast with optical

lithography which uses light to form patterns needed for materials deposition on the

wafer, electron beam lithography uses a focused beam of electrons for the same

purpose. Because of the shorter wavelength (0.2-0.5 Å) exhibited by the EBL systems,

electron beam lithography offers higher patterning resolution than optical lithography

which is limited by diffraction.

The primary advantage of electron beam lithography is that it is one of the ways to

beat the diffraction limit of light and make features in the nanometer regime. This form of maskless lithography [18] has found wide usage in mask-making used in photolithography, low-volume production of semiconductor components, and research and development.

2.8.1 Electron energy deposition in matter

The primary electrons in the incident beam lose energy upon entering a material through inelastic scattering or collisions with other electrons. In addition to producing secondary electrons, primary electrons from the incident beam with sufficient energy to penetrate the photoresist can be multiply scattered over large distances from underlying films and/or the substrate. This leads to exposure of areas at a significant distance from the desired exposure location. For thicker electrons, as the primary electrons move forward, they have an increasing opportunity to scatter laterally from the beam-defined location. This scattering is called forward scattering. Sometimes the primary electrons are scattered at angles exceeding 90 degrees, i.e., they no longer advance further into the resist. These electrons are called backscattered electrons and have the same effect as long-range flare in optical projection systems. A large enough dose of backscattered electrons can lead to complete exposure of resist over an area much larger than defined by the beam spot. The smallest features produced by
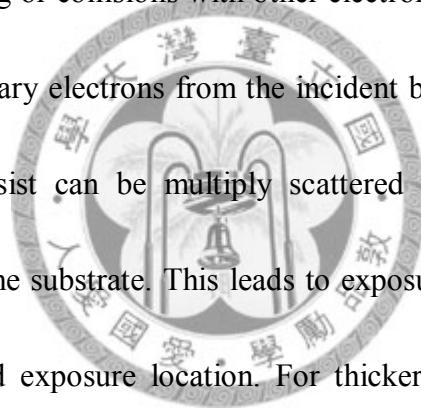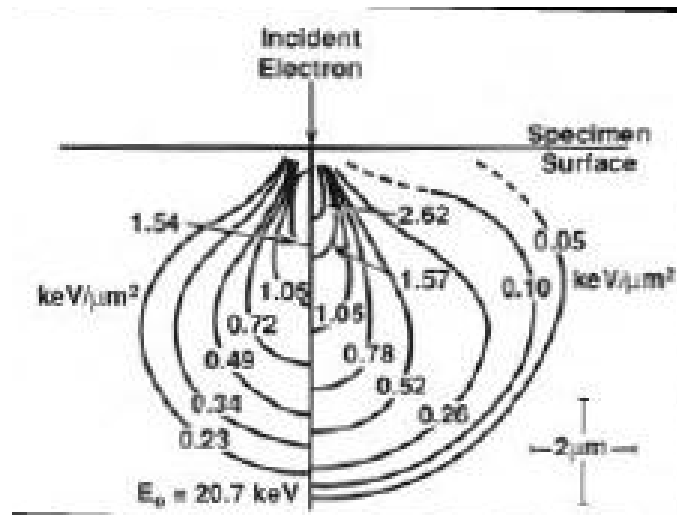
Fig. 2.8.1 Proximity effect due to electron scattering. (D. F. Kyser and N. S.

Viswanathan, J. Vac. Sci. Technol. **12**(6), 1305 (1975))
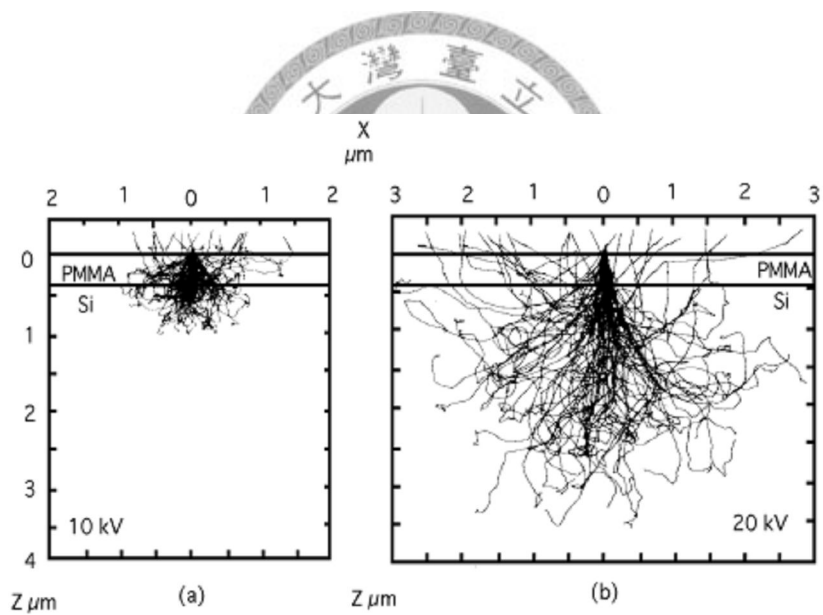
Fig. 2.8.2 Monte Carlo simulation of electron scattering in resist on a silicon substrate

at (a) 10 kV and (b) 20 kV. (D. F. Kyser and N. S. Viswanathan, J. Vac. Sci.

Technol. **12**(6), 1305 (1975))

electron beam lithography have generally been isolated features, as nested features

exacerbate the proximity effect, whereby electrons from exposure of an adjacent

region spill over into the exposure of the currently written feature, effectively

enlarging its image, and reducing its contrast, i.e., difference between maximum and

minimum intensity [19]. Figure 2.8.1 shows the proximity effect of interaction

volume and figure 2.8.2 shows electron scattering in the matter [20].

2.9 The Schottky barrier diode [21]

The ideal energy-band diagram for a particular metal and n-type semiconductor

before making contact is shown in figure 2.9.1(a). The parameter ϕ_m is the metal

work function, ϕ_s is the semiconductor work function, and χ is the electron

affinity. In figure 2.9.1(a), we have assumed that $\phi_m > \phi_s$. The ideal

thermal-equilibrium metal-semiconductor energy-band diagram is shown in figure

2.9.1(b). Before contact, the Fermi level in the semiconductor was above that in the

metal. In order for the Fermi level to become a constant through the system in the

thermal equilibrium, electrons flow into the lower energy states in the metal from the

semiconductor. Hence positive charged donor atoms remain in the semiconductor,

creating a space charge region. The parameter ϕ_{BO} is the barrier height of the

semiconductor contact, the barrier is known as the Schottky barrier and is given by

$\phi_{BO} = (\phi_m - \chi)$. On the semiconductor side, V_{bi} is the built-in potential barrier, and

the built-in potential barrier is given by $V_{bi} = \phi_{BO} - \phi_n$.

The energy-band diagrams for the reverse and forward bias are shown in Figures

2.9.2(a) and 2.9.2(b), where V_R is the magnitude of the reverse-bias voltage and V_a is

the magnitude of the forward-bias voltage.

2.10 Metal-semiconductor ohmic contacts [21]

Figure 2.10.1 shows an ideal contact between a metal and a p-type semiconductor.

Figure 2.10.1(a) shows the energy levels before contact for the case when $\phi_m > \phi_s$.

When contact is made, electrons from the semiconductor will flow into the metal to

achieve thermal equilibrium, leaving behind more empty states, or holes. The excess

concentration of holes at the surface makes the surface of the semiconductor more p

type. Electrons from the metal can readily move into the empty states in the

semiconductor. This charge movement corresponds to holes flowing from the

semiconductor into the metal. This junction is an ohmic contact.
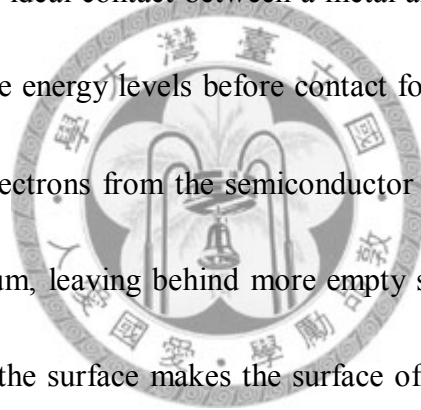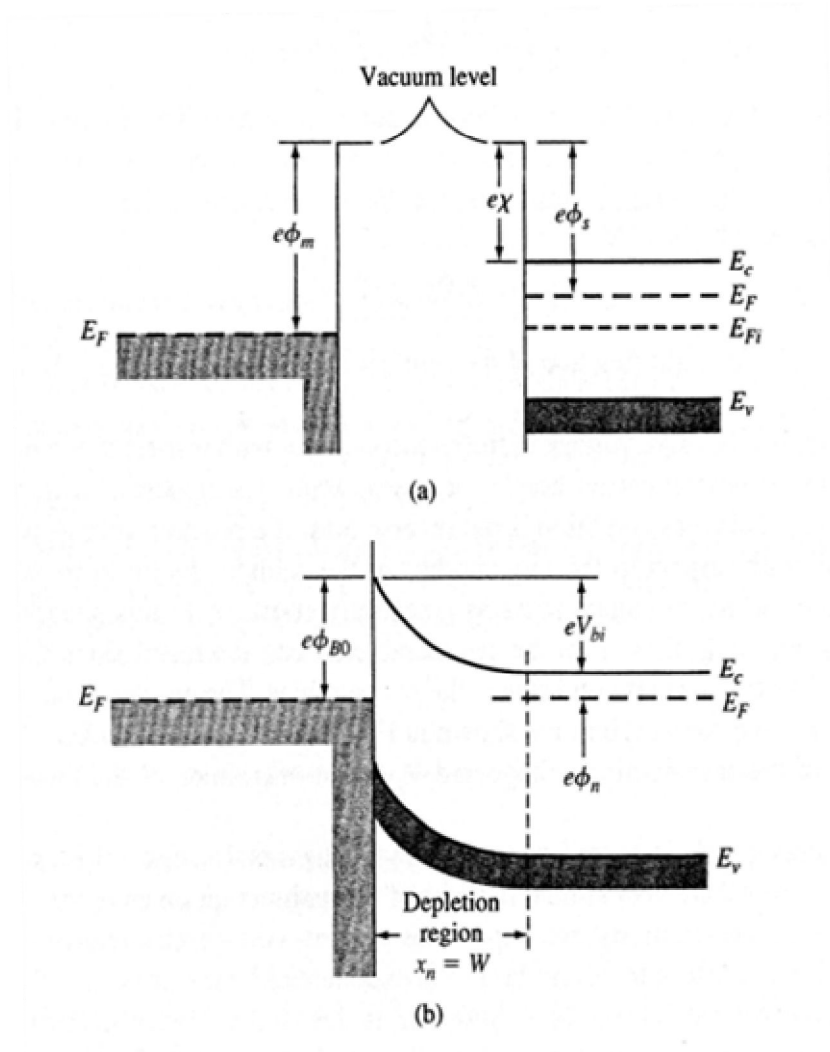
Fig. 2.9.1 (a) Energy-band diagram of metal and semiconductor before contact； (b)

ideal energy-band diagram of a metal-n-semiconductor junction for $\phi_m >$

ϕ_s. (Donald A. Neamen, Semiconductor Physics and Devices. P.327-476)

Fig. 2.9.2 Ideal energy-band diagram of a metal-semiconductor junction (a) under

reverse bias and (b) under forward bias. (Donald A. Neamen,

Semiconductor Physics and Devices. P.327-476)
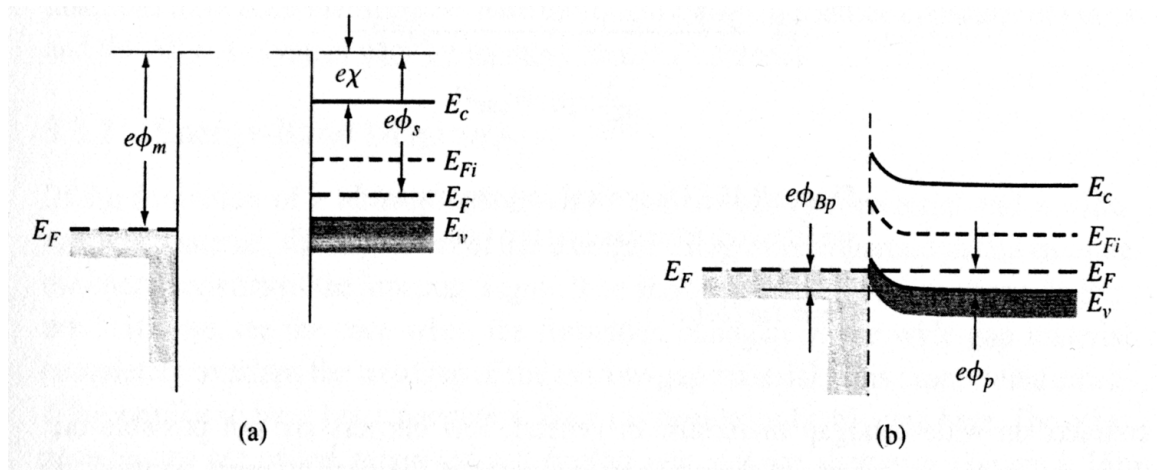
Fig. 2.10.1 Ideal energy-band diagram (a) before contact and (b) after contact for a

metal-p-semiconductor junction for $\phi_m > \phi_s$. (Donald A. Neamen,

Semiconductor Physics and Devices. P.327-476)

2.11 The energy-band diagram of the metal-oxide-semiconductor

field-effect transistor [21]

Figure 2.11.1 shows the structure of basic MOS. The parameter t_{ox} in the figure is the thickness of the oxide and ε_{ox} is the permittivity of the oxide. The traditional MOS structure is obtained by depositing a layer of silicon dioxide on the doped silicon substrate, and then a layer of metal is evaporated on back of the substrate as a gate.

The energy-band diagram of the MOS structure with the p-type substrate, for the case when a negative voltage is applied to the top of the metal, is shown in the figure 2.11.2(a). Figure 2.11.2(b) shows the energy-band diagram of the MOS structure with the p-type substrate when a positive voltage is applied to the gate. As a result, the conduction and valence band edges bend as shown in the figure 2.11.2 when a negative or positive voltage is applied to the gate. The induced space charge width is x_d. When a still large positive voltage is applied to the gate of the MOS structure, an inversion layer of electrons at the oxide-semiconductor interface is created. This result implies that the surface of semiconductor has been inverted from a p-type to an n-type semiconductor.
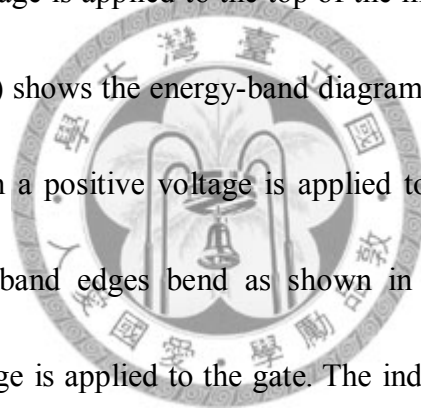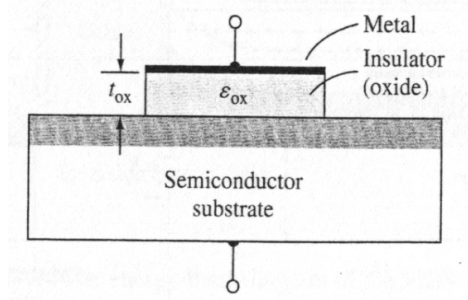
Fig. 2.11.1 Basic MOS capacitor structure.
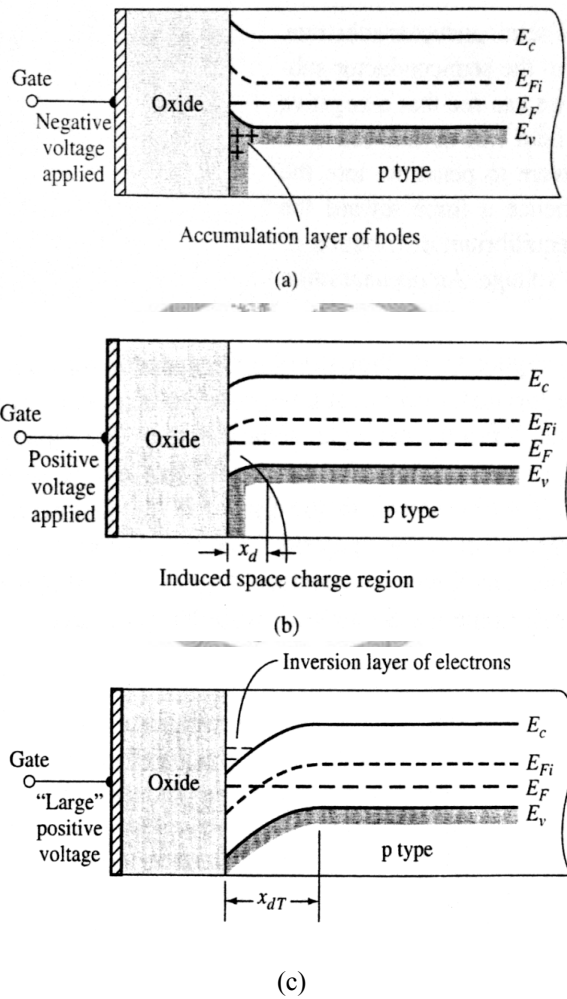
Fig. 2.11.2 Energy-band diagram of an MOS structure with a p-type substrate for

(a) a negative gate bias and (b) a moderate positive gate bias (c) a large

positive gate bias. (Donald A. Neamen, Semiconductor Physics and

Devices. P.327-476)

References

[1] M. H. Huang, Y. Wu, H. Feick, N. Tran, E. Weber and P. D. Yang, Adv. Mater. **13**, 113 (2001).

[2] M. H. Huang, S. Mao, H. Feick, H. Yun, Y. Wu, H. Kind, E. Weber, R. Russo, and P. D.Yang. Science **292**, 1897 (2001).

[3] Z. W. Pan, Z. R. Dai, and Z. L. Wang, Science. **291**, 1947 (2001).

[4] J. Q. Hu, Q. Li, N. B. Wong, C. S. Lee, and S. T. Lee, Chem. Mater. **14**, 1216 (2002).

[5] J. C. Hulteen, C. R. Martin, and J. Mater. Chem. **7**, 1075 (1997).

[6] Y. Li, G. W. Meng, L. D. Zhang, and F. Phillipp, Appl. Phys. Lett. **76**, 2011 (2000).

[7] R. S. Wagner, and W.C. Ellis, Appl. Phys. Lett., **4**, 89(1964).

[8] A. M. Morales and C. M Lieber, Science. **279**, 208 (1998).

[9] Y. Wu and P. Yan,. J. Am. Chem. Soc. **123**, 3165 (2001).

[10] G. B. Stringfellow, Organometallic Vapor-Phase Epitaxy：Theory and Practice, 2nd ed. Academic Press (1999).

[11] T. H. Gfroerer, in Encyclopedia of Analytical Chemistry, 9209 (2000).

[12] G. I. Goldstein, D. E. Newbury, P. Echlin, D. C. Joy, C. Fiori, and E. Lifshin, Scanning electron microscopy and X-ray microanalysis, Plenum Press, New York and London (1981).

[13] R. A. Stradling and P. C. Klipstein, Growth and Characterisation of Semiconductors (Hilger, 1990).

[14] V. K. Zworykin, J. Hiller, and R. L. Snyder, ASTM Bull. **117**, 15 (1942).

[15] http://www.eserc.stonybrook.edu/ProjectJava/Bragg/

[16] R. Nana, Taking the confusion out of confocal microscopy. Bio Teach Journal. **1**, 75-80 (2003).

[17] L. R. Qiu, X. M. Ding, and J. Liu, Confocal Measurement Approach for enhancing lateral resolution using a phase-only pupil. J. Phys. Conf. Ser. **13**, 422-425 (2005).

[18] M. Klosner and K. Jaina, Appl. Phys. Lett. **84,** 2880 (2004).

[19] S. Rizvi et al. Handbook of Photomask Manufacturing Technology, (Taylor & Francis Group, (2005).

[20] D. F. Kyser and N. S. Viswanathan, J. Vac. Sci. Technol. B, **12**(6), 1305 (1975).

[21] Donald A. Neamen, Semiconductor Physics and Devices. P.327-476
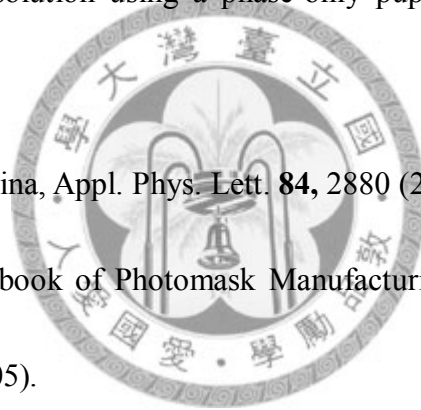
Chapter 3

Sample preparation

3.1 Growth of ZnO nanowires and ZnO/ZnTe core-shell nanowires

A two-step synthesis was used to fabricate the ZnO/ZnTe core-shell nanowire arrays. In the first step, the ZnO nanowires were grown for 40 minutes at T= 930 °C in a furnace by chemical vapor deposition with gold as catalyst. The detailed mechanism is shown in figure 3.1.1. ZnO and carbon powders mixed in the weight ratio of 7：1 was chosen as reactant materials. High-purity argon gas (99.99％) was introduced into the quartz tube at a constant flow rate of 100 sccm at a growth temperature of 930 ℃.
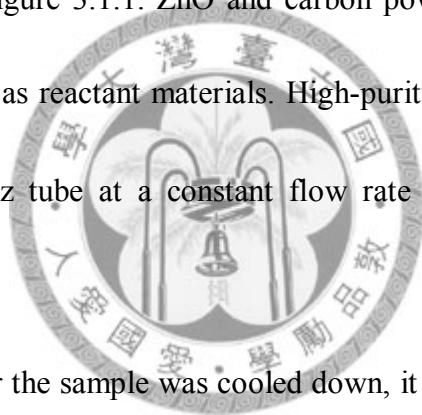
In the second step, after the sample was cooled down, it was then transferred to the MOCVD chamber to deposit ZnTe shell on ZnO nanowire surface for 150-600 seconds at T= 550 °C. DMZn and DMTe were used as precursors, the molar flow rate of DMZn and DMTe is 1：2 and the reactor pressure were kept at 760 torr during the growth process. Finally, the ZnO/ZnTe core-shell structure was fabricated by using CVD and MOCVD methods. The illustration of the core-shell nanowires is shown in figure 3.1.2.
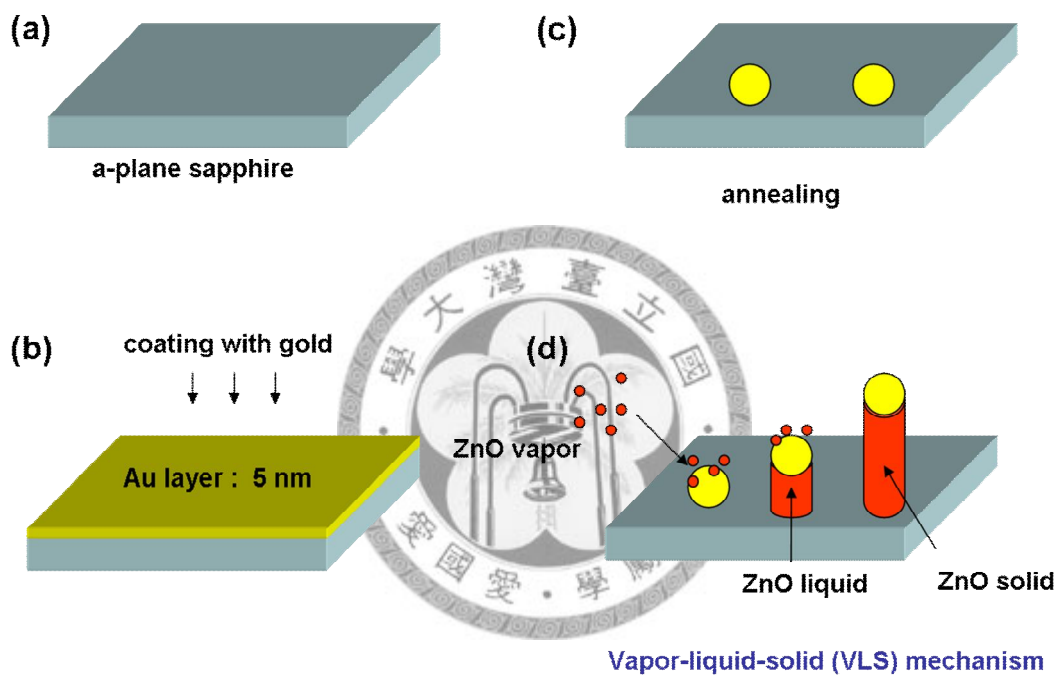
Fig. 3.1.1 (a) ~ (d) Schematic diagrams of ZnO nanowires grown on a-plane sapphire

by using CVD with gold as catalyst.
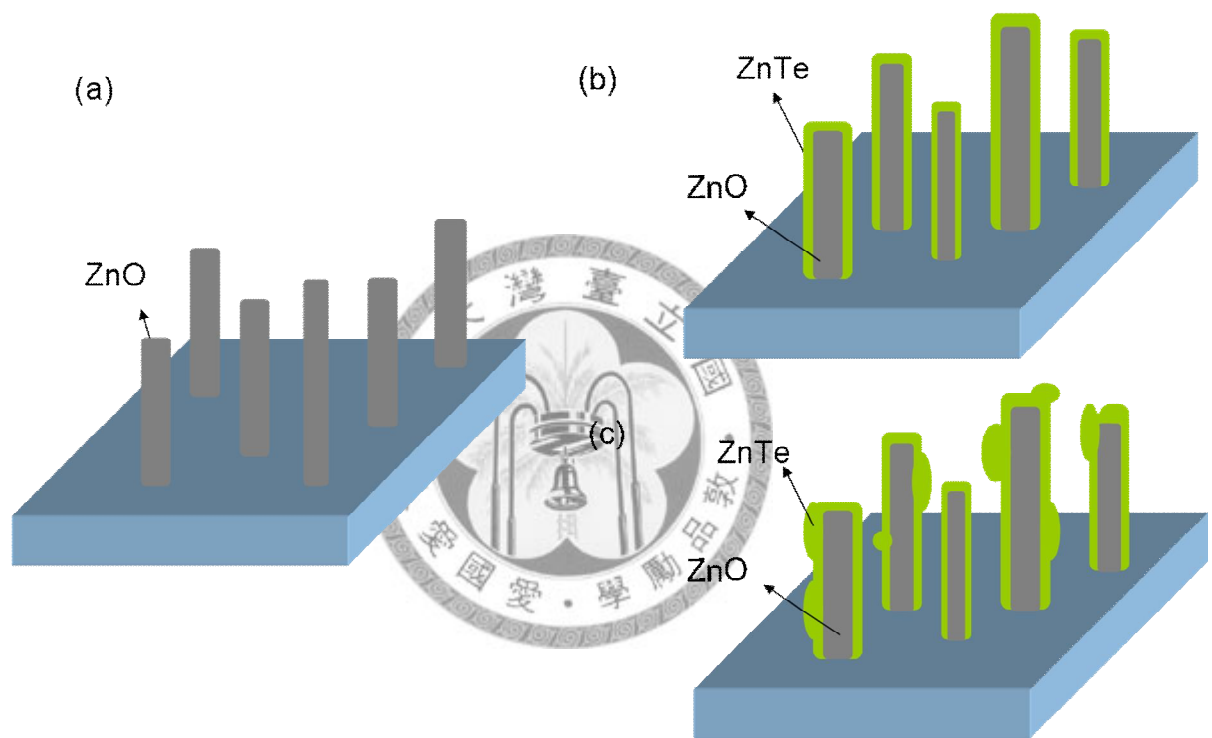
Fig. 3.1.2 Schematic diagram of growing ZnO/ZnTe core-shell nanowires (a) ZnO

nanowires were grown on a-plane sapphire by using CVD. (b) and (c) The

ZnTe shell was grown on the ZnO surface by using MOCVD.

3.2 Fabrication of single ZnO/ZnTe core-shell nanowire field-effect transistor

In order to study the electric properties of a single core-shell nanowire, we fabricate a field-effect transistor (FET) device by using photo lithography and e-beam lithography. After the growth of the ZnO/ZnTe core-shell nanowire, the nanowire was then placed on top of a 300 nm SiO_2 layer which in term was on top of a p-type Si substrate to form a field effect transistor with the heavily doped silicon substrate served as a metal gate. Before scraping the core-shell nanowires onto the SiO_2/Si substrate, we use photo lithography to make electrode and alignment marks and then sputter Ti/Au to the substrate. The following procedures are used and figure3.2.1 is the schematic diagram of the procedures：
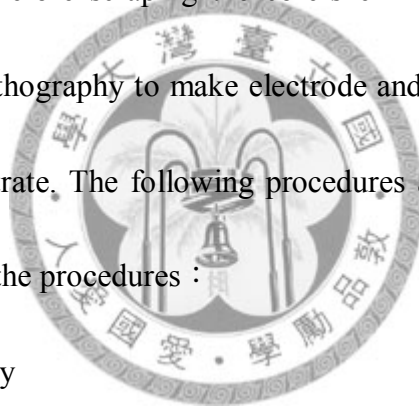
Step 1：Photo Lithography

(1) Clean the substrate by using GP solution, acetone and DI water.

(2) Spin coating with photoresistor DMP3020.

   (First, the sample is controlled by 3000 rpm for 10 seconds. Second, it is controlled by 5000 rpm for 30 seconds)

(3) Soft Bake：110 ℃ for 10 minutes.

(4) Exposure：32 seconds.

(5) Development：20 seconds.
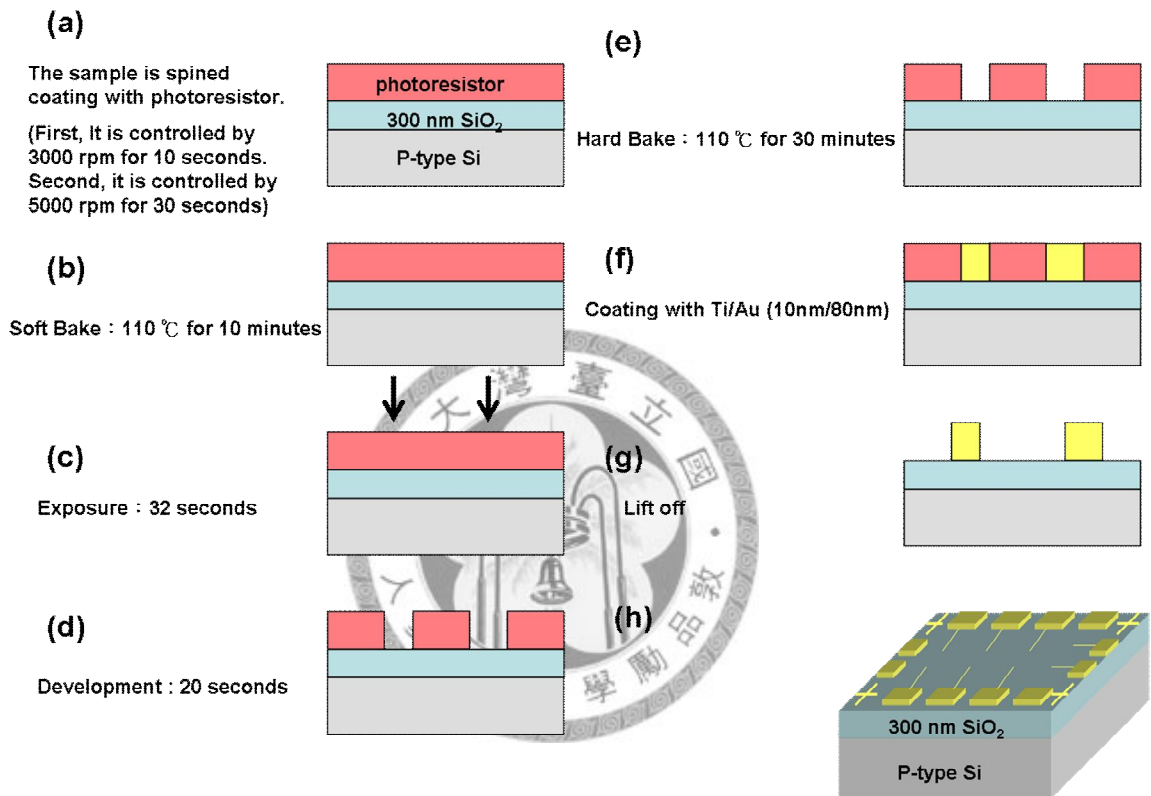
Fig 3.2.1 Schematic diagram of the photo lithography process and lift-off technique.

(6) Hard Bake：110 ℃ for 30 minutes.

(7) Sputter Ti/Au (10 nm/80 nm).

(8) Lift off.

The square shown in figure 3.2.2(a) is of size 75×75 μm2, and the alignment marks are at the outer edges. Then the core-shell nanowires were scraped onto the square, as can be observed in figure3.2.2(b). We can measure their position relative to the alignment marks as shown in figure 3.2.2(b). Then metallic electrodes consisting of Ti/Au were deposited on the two ends of the nanowire by an electron beam evaporator and defined as source and drain electrodes by using e-beam lithography and lift-off process.

The process for e-beam lithography is as following：

Step 2：Electron Beam Lithography

(1) Spin coating with ZEP520.

(step1：500 rpm for 5 seconds； step 2：5000 rpm for 90 seconds)

(2) Baking 180 ℃ for 5 minutes.

(3) Exposure by E-beam Lithography.

(4) Development (20 seconds ~ 120 seconds).

(5) Sputter Ti/Au (10 nm/80nm).

(6) Lift off.
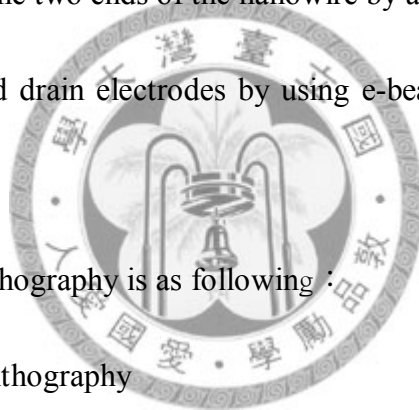
After these processes, the single core-shell nanowire FET was successfully fabricated, as is shown in figure 3.2.2(d). The electric properties of the core-shell nanowires FET are discussed in chapter 5.

3.3 Growth of ZnO nanowires and ZnO/ZnSe core-shell nanowires

The methods used for growing ZnO nanowires and ZnO/ZnSe core-shell nanowires are also the CVD and MOCVD growth methods. The growth time of the ZnO nanowires is for 8 hrs in a CVD system. During the growth, high-purity argon gas (99.99％) was introduced into the quartz tube and the flow rate is set a 100 sccm at a growth temperature of 930 ℃. After the sample was cooled down, the sample was then transferred to the MOCVD chamber to deposit ZnSe shell on ZnO nanowire surface for 25 minutes at T= 550 ℃ and the growth pressure were kept at 760 torr. Dimethylzinc (DMZn) and Dimethylselenide (DMSe) were used as precursors, and the molar flow rate of DMZn and DMSe is set at 1：2 during the growth.
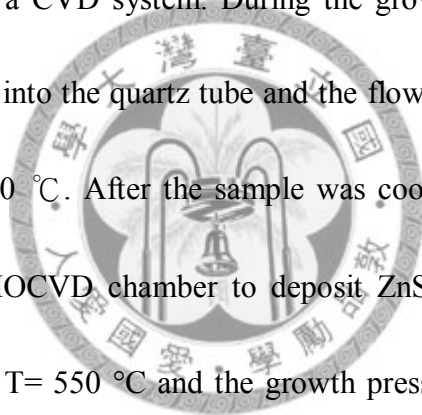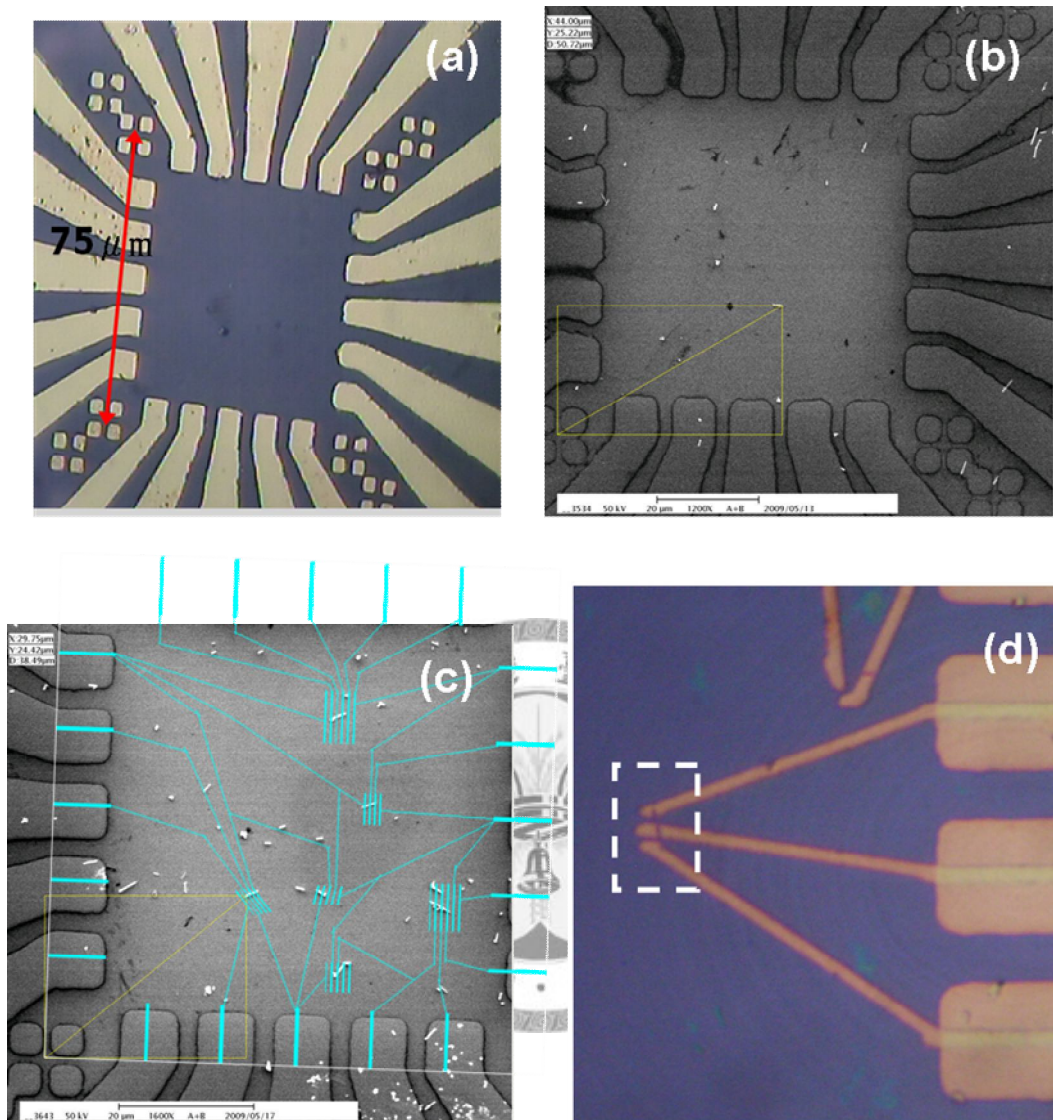
Fig 3.3.1 Square shown in figure (a) is of size 75×75 μm^2, and alignment marks are at

the outer edges. The core-shell nanowires were scraped onto the square

as can be seen in the figure (b). The metallic electrodes were deposited on the

two ends of the nanowire by using e-beam lithography and lift-off process as

were shown in figure (c) and (d).

Chapter 4

Growth and characterization of type-II ZnO/ZnTe core-shell nanowire arrays

4.1 Introduction

Recently, quasi-1D systems might be the optimized choice for making opto-electronic devices due to the advantage of the reduced dimensionality. Besides, to synthesis core-shell nanowires [1-3] play an important part in quai-1D systems because they can reinforce the functions of nanowires synthesized by one material. In this study, we report our studies on the growth and characterization of the vertically aligned ZnO/ZnTe core-shell nanowires. Chemical vapor deposition and metal-organic chemical vapor deposition were used to grow ZnO core and ZnTe shell and our results revealed the ZnO/ZnTe core-shell structures are good crystalline quality.

4.2 Experimental details

The process for synthesizing the ZnO core and the ZnTe shell were motioned in section 3.1. The growth time of ZnO core is for 40 minutes at T=930 ℃. The ZnTe shell was grown at T=530 ℃ for 150-600 seconds. The morphology and size

distribution of the ZnO/ZnTe core-shell nanowire arrays were studied by scanning electron microscopy (SEM), the crystal structures were examined by x-ray diffraction (XRD) and transmission electron microscopy (TEM).

4.3 Results and discussion

Figure 4.3.1(a) shows the tilt-view SEM image of ZnO nanowire arrays on the sapphire substrate. This image revealed that the ZnO wires are vertically aligned, the length of nanowire is around 1~2 μm and the diameter are in the range of 70-100 nm. The SEM picture of the core-shell ZnO/ZnTe nanowires with coating time of 600sec is shown in figure 4.3.1(b) and the inset is enlargement of one of the nanowire. Comparing figure 4.3.1(a) with figure 4.3.1(b), it was found that the surface of ZnO wires became rougher after the growth of ZnTe shell, and the diameter of the nanowire increase from 70-100 nm to 150-300 nm. From the images it can be observed that ZnTe shell was successfully grown on the ZnO nanowire in large area. The thickness of the ZnTe shell grown on the ZnO nanowire core was controlled by adjusting the coating time. Figure 4.3.2 shows the TEM images of ZnO/ZnTe core-shell nanowire synthesized using different ZnTe shell coating time. Compare figure 4.3.2(a) with figure 4.3.2(b), we can find that when the depositing time of ZnTe shell was increased form 150 to 300 sec, the thickness of the ZnTe shell from 10 to 25
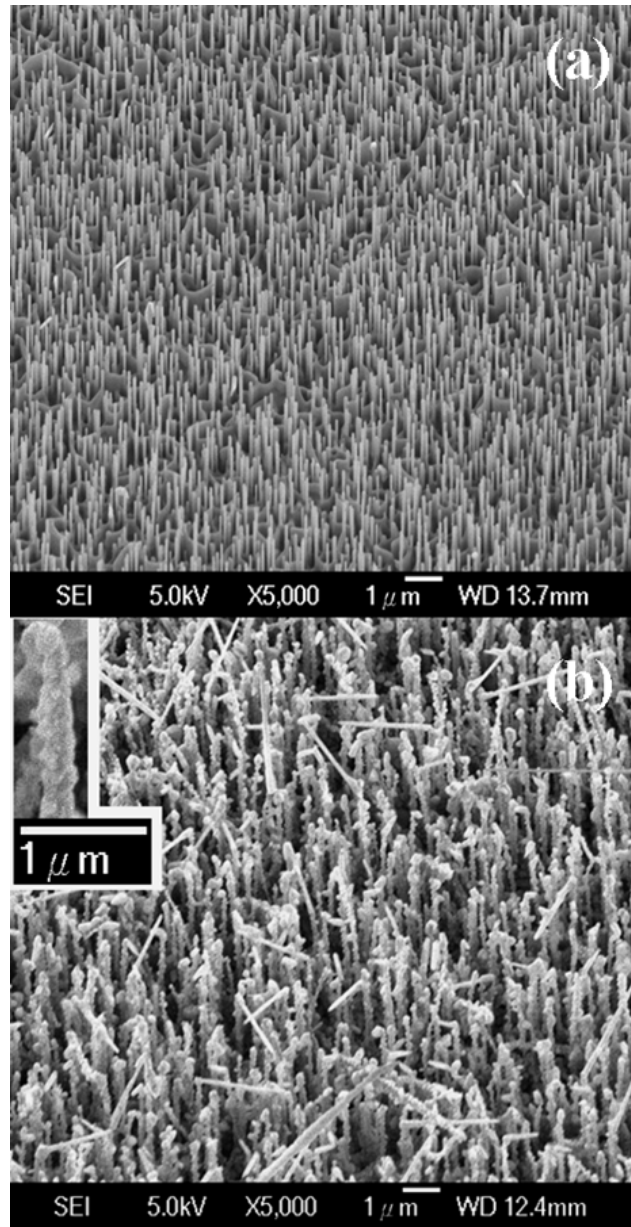
Fig. 4.3.1 Tilt-view SEM images of (a) aligned ZnO nanowire arrays (b) ZnO/ZnTe core-shell nanowires arrays with depositing time of 600 sec. The inset is high-magnification SEM image of a single ZnO/ZnTe core-shell nanowire.
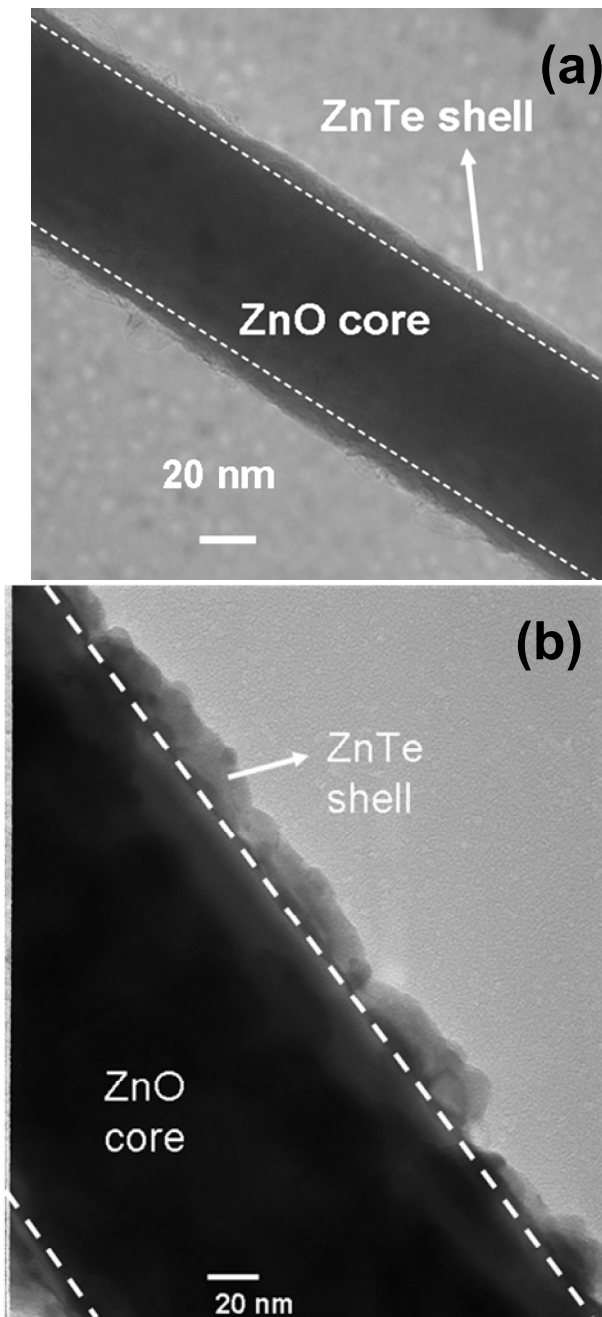
Fig. 4.3.2 (a) and (b) are the TEM images of ZnO/ZnTe core-shell nanowire and the

growth time of ZnTe shell are 150 and 300 sec for (a) and (b), respectively.

nm. We can also find in these figures that when the depositing time is short, the ZnO/ZnTe core-shell nanowire has a better surface morphology.

Figure 4.3.3 shows the XRD patterns of ZnO nanowires and ZnO/ZnTe core-shell nanowire arrays with ZnTe depositing time of 600 sec. In figure 4.3.3(a) the peak occurs at $2\theta=34.2°$ is the diffraction peak from the (002) plane of the ZnO nanowires with wurtzite structure (a = 0.3253 nm and c = 0.5213 nm) and it also indicated that the ZnO nanowires were oriented in the c-axis direction. The ZnO (101) peak in the figure is attributed to the diffraction peak from the thin layer of ZnO which was grown before ZnO nanowires. From the narrow half width of the XRD peak, we conclude that the ZnO nanowires have good crystalline quality. The XRD result of the ZnO/ZnTe core-shell structures is shown in figure 4.3.3(b). Although the (002) and (101) peaks from ZnO are still observable in this figure, the spectra is now dominated by the diffraction pattern from ZnTe. The diffraction peaks at 25.0°, 41.7° and 49.4° are attributed to the diffraction from the (111), (220) and (311) planes of ZnTe with zinc-blende structure (a = 0.610 nm), respectively. As the diffraction peak from (111) plane has much higher intensity than that from the (220) and (311) plane, the majority ZnTe layer are in [111] direction. From the quality of the diffraction peaks we can also conclude that the crystalline quality of the ZnTe shell is also of good quality. As the position of the diffraction peaks of ZnTe shell is the same as the position of the
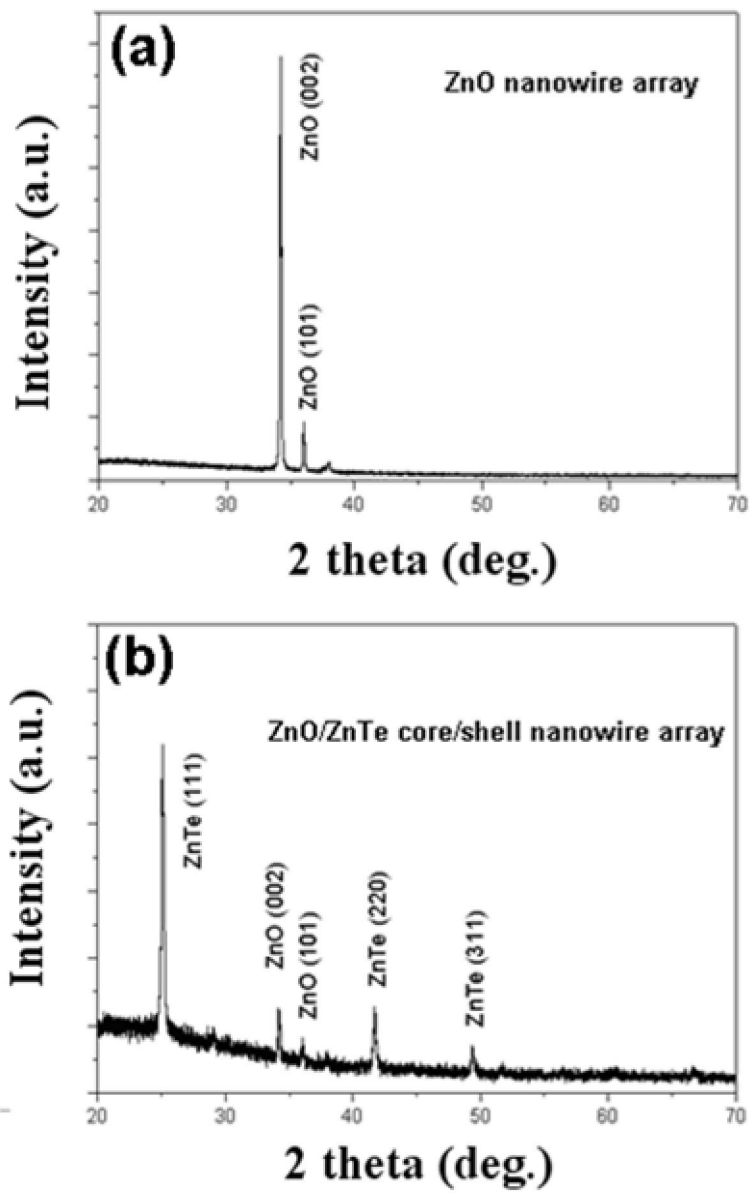
Fig. 4.3.3 XRD patterns of (a) ZnO nanowire arrays (b) ZnO/ZnTe core-shell

nanowire arrays with coating time of 600 sec.

diffraction peaks of bulk ZnTe and the ZnTe layer is apparently fully relaxed in the ZnO/ZnTe nanowires. These results are consistent with the results obtained from the SEM image that a layer of ZnTe with thickness of around 100 nm was coated on the surface of the ZnO nanowires.

High-resolution TEM characterization was carried out to study the crystal structure of ZnO nanowire core and to obtain more detailed information about the structure of ZnTe shell. Figure 4.3.4(a) shows the HRTEM image of ZnO nanowire. It is clear from this figure that the nanowire is a single crystal and the separation between the crystallographic planes is 0.26 nm. This separation corresponds to the spacing between (002) planes of ZnO with wurtzite structure, and it confirms the growth direction of the ZnO nanowires was along the [002] direction. The inset of figure 4.3.4(b) shows a typical low-magnification TEM image of the core-shell nanowire. After the ZnO nanowire was coated with ZnTe shell, the ZnO nanowire not only increases its diameter but also have ZnTe grains attached to its surface. We can found from the high-resolution TEM image shown in figure 4.3.4(b) that the distance between the crystallographic planes is 0.35 nm, which corresponds to the spacing between (111) planes of zinc-blende ZnTe. The dark region in the figure is attributed to the overlap between the signals from ZnTe shell and underlying ZnO core. The TEM results demonstrate that the shell is indeed a ZnTe layer with good crystalline
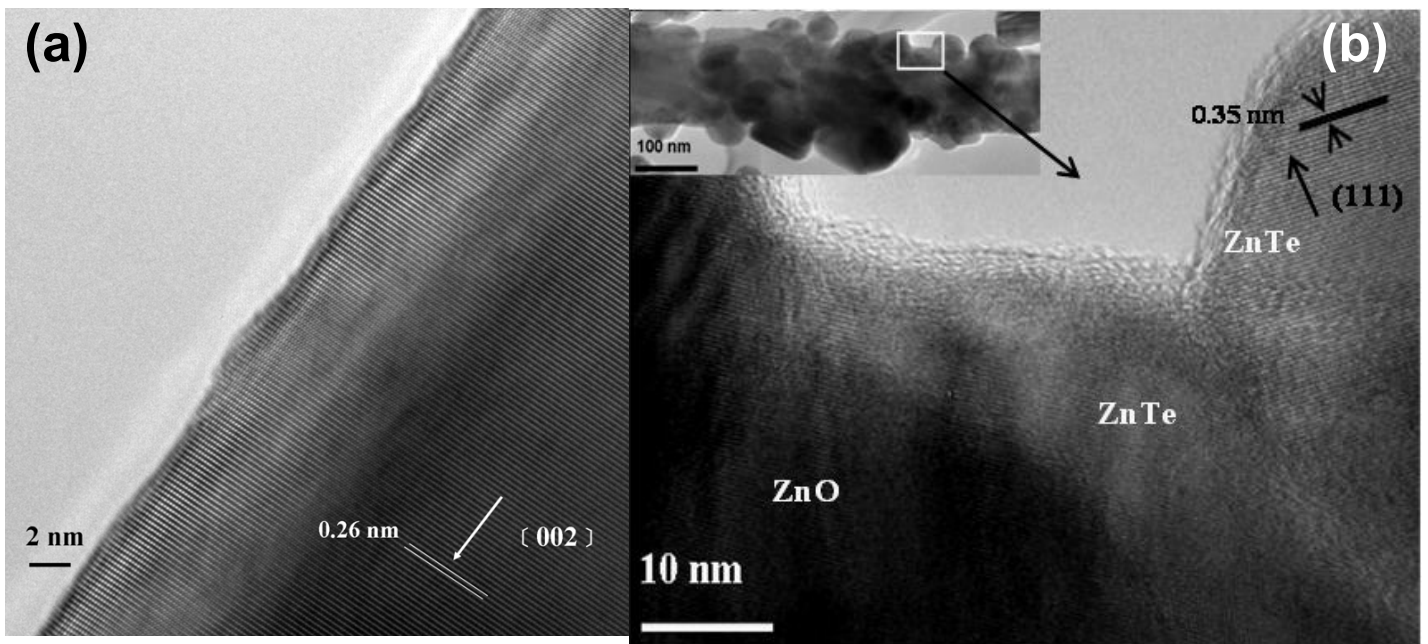
Fig. 4.3.4 (a) High-resolution TEM image of the ZnO nanowire core (b) is HRTEM

image of the ZnTe grain corresponding to the rectangle in the TEM image

in the inset; the inset is low-magnification TEM image of the ZnO/ZnTe

core-shell nanowire.

quality.

4.4 Conclusion

In conclusion, large area, vertically aligned ZnO/ZnTe core-shell nanowire arrays were successfully grown by using CVD and MOCVD for the growth of ZnO core and ZnTe shell and their crystal structures are examined in details. SEM, XRD and TEM characterization indicate that the ZnO core has wurtzite structure, ZnTe shell has zinc-blende structure and both materials have good crystalline quality.

References

[1] W. U. Huynh, J. J. Dittmer, and A. P. Alivisatos, Science. **295**, 2425 (2002).

[2] W. U. Huynh, J. J. Dittmer, W. C. Libby, G. L. Whiting, and A. P. Alivisatos, Adv. Funct. Mater. **13**, 73 (2003).

[3] Y. Kang, N. G. Park, D. Kim, Appl. Phys. Lett. **86**, 113101 (2005).

[4] M. Law, L. E. Greene, J.C. Johnson, R. Saykally, and P. Yang, Nat. Mater. **4**, 455 (2005).

[5] J. B. Baxter, and E. S. Aydil, Appl. Phys. Lett. **86**, 053114 (2005).

[6] W. U. Huynh, J. J. Dittmer, and A. P. Alivisatos, Science. **295**, 2425 (2002).

[7] W. U. Huynh, J. J. Dittmer, W. C. Libby, G. L. Whiting, and A. P. Alivisatos, Adv. Funct. Mater. **13**, 73 (2003).

[8] Y. Kang, N. G. Park, and D. Kim, Appl. Phys. Lett. **86**, 113101 (2005).

[9] H. Zhong, Y. Zhou, Y. Yang, C. and Yang, Y. Li, J. Phys. Chem. C **111**, 6538 (2007).
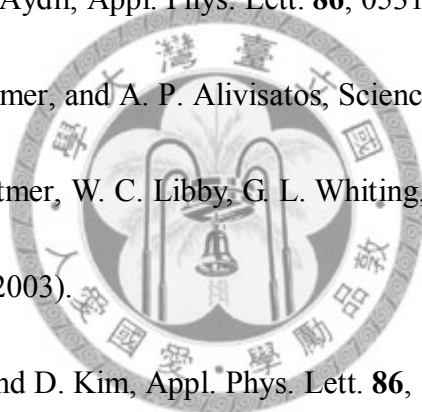
Chapter 5

The optical properties of ZnO/ZnTe core-shell nanowires

and single core-shell nanowire field effect transistor

5.1 Introduction

Among one-dimensional structures, ZnO has been the most extensively studied system because good quality vertically aligned ZnO nanowires can be easily grown with simple and inexpensive methods [1-5]. However, in order to improve the stability of the performance of the ZnO-nanowire-based devices, it is desirable to passivate the surface of the ZnO nanowires by using core-shell structures. This structure is also a novel method which can be applied to measure the electric properties of nanotubes because the carrier can be confined in the shell. So far, there are only limited reports on optical properties and electrical transport properties of the ZnO-based II-VI core-shell nanowires. In this paper we report the growth and characterization of the ZnO/ZnTe core-shell nanowires, and the electrical properties of the field effect transistor (FET) made by using the ZnO/ZnTe core-shell nanowire.

5.2 Experimental details

The process for fabricating ZnO/ZnTe core-shell nanowires were described in

chapter 4. The morphology and size distribution of the ZnO/ZnTe core-shell nanowires were studied by scanning electron microscopy (SEM). The optical properties of the ZnO/ZnTe core-shell nanowires were measured by Raman scattering, transmission and laser scanning confocal microscopy at room temperature. Raman scattering was measured by using the 325 nm light emitted from a He-Cd laser as excitation source. For the optical transmission measurement, a Xe lamp was used as light source. Laser scanning confocal microscopy was measured by using 488 nm light emitted from an Ar^+ laser as excitation source.

For the fabrication of the single-nanowire FET, ZnO/ZnTe nanowire was placed on top of a 300 nm SiO_2 layer which in term was thermally grown on top of a p^+-Si substrate to form FET with the heavily doped silicon substrate served as a metal gate. Ti/Au electrodes defined by standard e-beam photolithography and lift-off techniques were used to serve as metallic source and drain contacts on two ends of the ZnO/ZnTe core-shell nanowire.

5.3 Results and Discussion

Figure 5.3.1(a) shows the tilt-view SEM image of the as-grown ZnO nanowires on the a-plane sapphire substrate. We can find in this figure that the length of the ZnO nanorwire is around 5~10 μm long and the diameter are in the range of 70-100 nm.

The Au nanoparticle on the tips of the ZnO nanowires indicates the growth mode is

vapor–liquid–solid (VLS) growth [6, 7]. Figure 5.3.1(b) is the SEM image of

ZnO/ZnTe core-shell nanowires. Comparing figure 5.3.1(a) with figure 5.3.1(b), we

can find that the surface of ZnO nanowires became rougher after the growth of ZnTe

shell, and the diameter of the nanowires increase from 70-100 nm to 150-300 nm.

From these images we can conclude that ZnTe shell was successfully grown on the

ZnO nanowire surface.

It is known that Raman spectra are sensitivity to crystallization, structural disorder

and defects in nanostructures. Raman spectra taken with the ZnO nanowires and

ZnO/ZnTe nanowires are shown in figure 5.3.2 For the sample consisting of only ZnO

nanowires the spectrum is dominated by the ZnO LO phonon peak that occurs at 576

cm^{-1} (A$_1$ LO mode) [8, 9], and the peak position suggest that ZnO nanowires has good

crystallization. For the ZnO/ZnTe core-shell nanowires, the Raman spectrum is now

dominated by the signal originated from the ZnTe shell. There are three peaks in the

Raman spectrum for the ZnO/ZnTe core-shell nanowires. The peak at 176 cm^{-1}

corresponds to the ZnTe TO phonon emission [8], the peak at 206 cm^{-1} can be

attributed the ZnTe LO phonon emission and the third peak at 412 cm^{-1} are the two

LO phonon emission peak [10-13]. From the Raman spectra we can conclude that

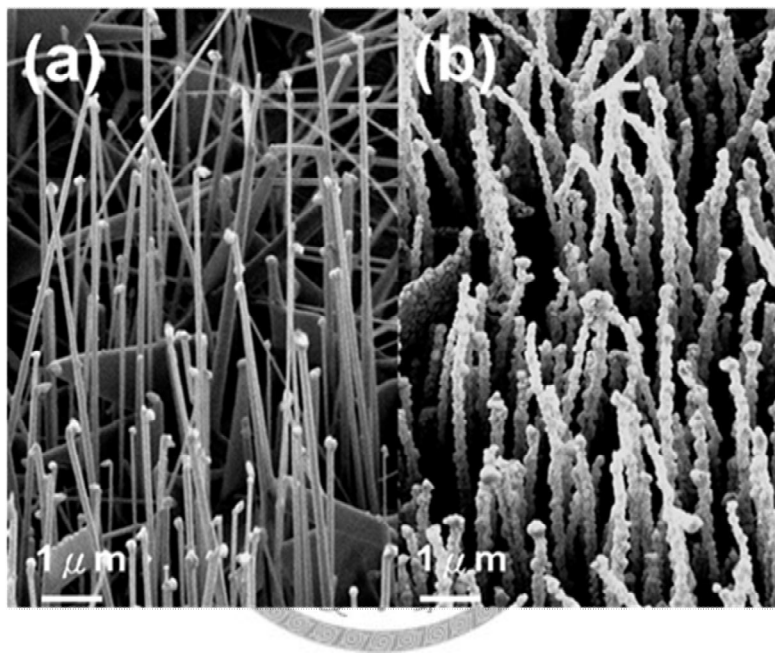ZnTe layer was grown on the surface of ZnO nanowires to form the ZnO/ZnTe

Fig. 5.3.1 (a) and (b) are the tilted-view SEM images of ZnO nanowire arrays and

ZnO/ZnTe core-shell nanowire arrays.
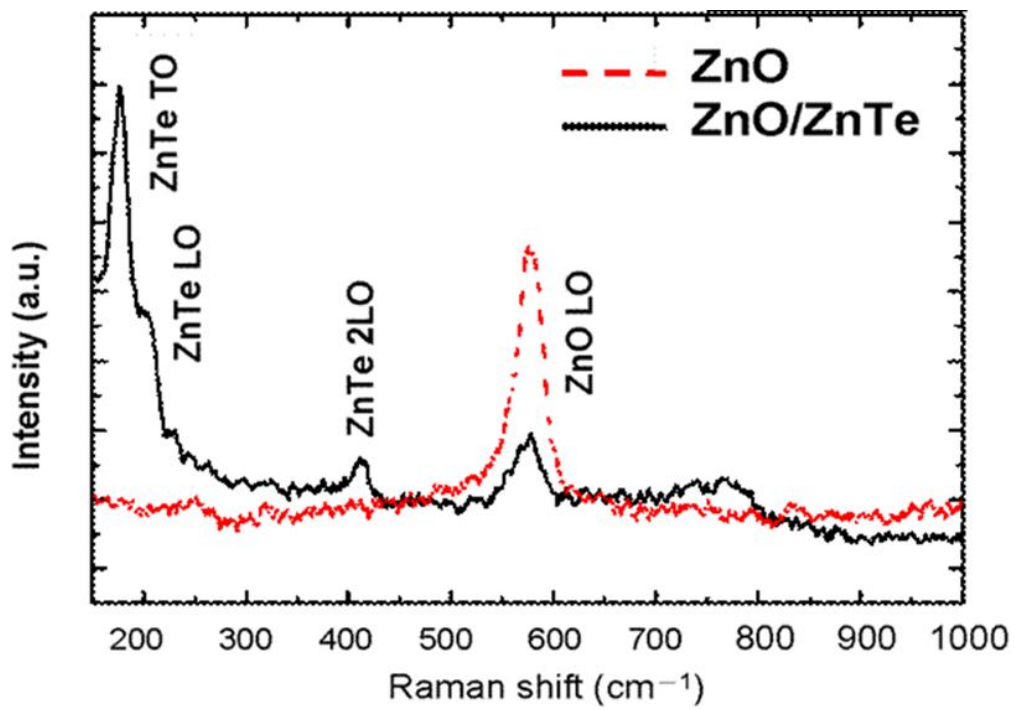
Fig. 5.3.2 Raman spectra of ZnO nanowires (dashed line) and ZnO/ZnTe core-shell

nanowires (solid line). The spectra were taken with He-Cd laser excited at

325 nm.

core-shell structures and both the ZnO and the ZnTe are of good crystalline qualities.

The results of the optical transmission measurement on the ZnO nanowires and ZnO/ZnTe core-shell nanowires are shown in figure 5.3.3. For the sample consists of only ZnO nanowires we could see that the sample is transparent in the visible range and the most importance feature in this transmission curve is the strong increase of light absorption near and above the energy gap of ZnO. But for the ZnO/ZnTe nanowires sample, we could find that the transmission curve is quite different from that of the ZnO nanowire sample. There are two sudden drops in the transmission curves of ZnO/ZnTe nanowires sample, one is near 375 nm and the other is near 550 nm, corresponding to the bandgap energy of ZnO and ZnTe, respectively. We also notice in this curve that the transmission intensity of the ZnO/ZnTe nanowires decrease gradually from 550 nm to 375 nm. For the staggered type-II band alignment, the band gap of the composite structure could be much smaller than the individual material that it was made of. In the case of ZnO/ZnTe the band gap is near 1.17 eV. Theoretical calculation taking into the proximity effect of the electron and hole wavefunctions in the nanostructure into consideration predicted that for the type-II core-shell nanostructure [14], the light absorption will start from the band gap energy and increase gradually as the photon energy increases, which is consistent with our results. In addition, we also found that the overall transmission intensity is much
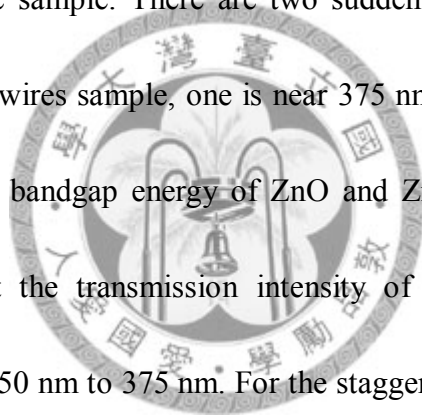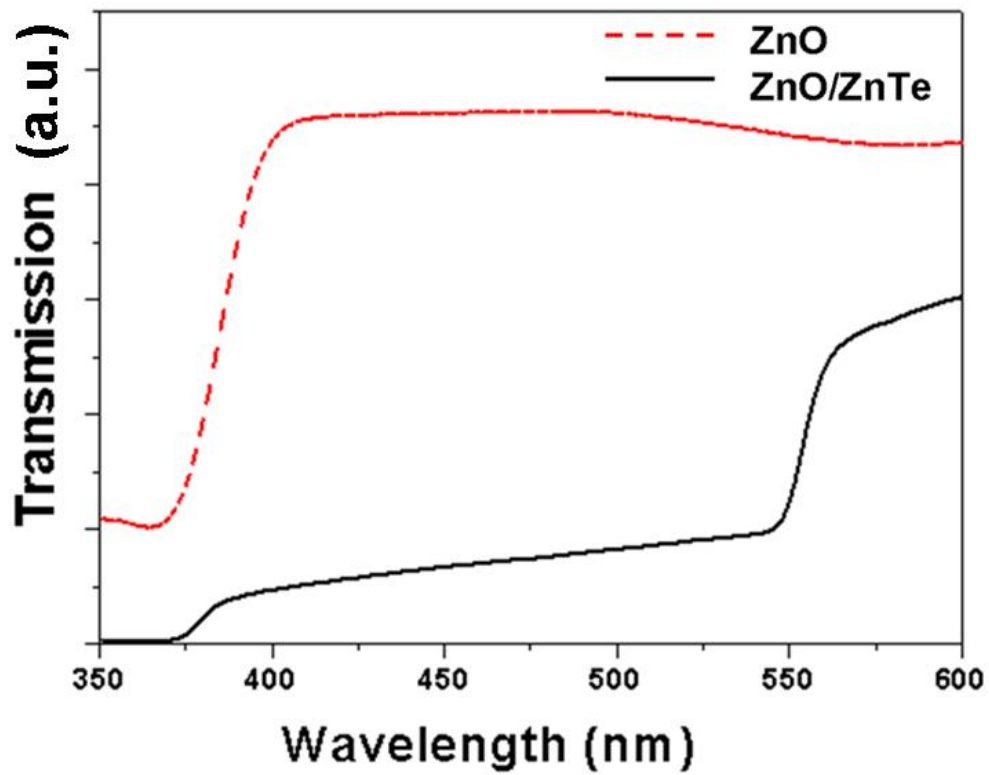
Fig. 5.3.3 Transmission spectra of ZnO nanowires (dashed line) and ZnO/ZnTe

core-shell nanowires (solid line).

smaller for the ZnO/ZnTe sample than that of the ZnO sample, indicating that the ZnO/ZnTe sample has light trapping effect.

Laser scanning confocal microscopy is a promising method for optical characterization of nanostructures; it can excite selective nanoscale region in the sample and can map out not only horizontal but also vertical luminescence properties of the nanowires. Figure 5.3.4(a) shows the top view of the photoluminescence image of the ZnO/ZnTe core-shell nanowires, and figure 5.3.4(b) shows the three-dimensional photoluminescence image of the nanowires when the image is tilted at 45° and the inset is the scale bar of the PL emission intensity. Figure 5.3.4(b) is constructed by stacking 40 images, each at a different depth, of the planar PL emission, after the laser scan. The PL emission in figure 5.3.4(b) detected at around 2.3 eV corresponds to the band gap emission of the ZnTe layer. The uniform PL emission intensity that can be observed in the 3D image indicates that the ZnO/ZnTe core-shell nanowires have good optical qualities and the ZnTe grown on ZnO are quite uniform.

To measure the electric properties of a single ZnO/ZnTe core-shell nanowire, ZnO/ZnTe nanowires were dispersed on a doped Si substrate with a SiO_2 layer and made into the FET as was described previously. Figure 5.3.5(a) shows a schematic diagram of the single ZnO/ZnTe core-shell nanowire FET device. Figure 5.3.5(b) is

Fig. 5.3.4 (a) Top view of the photoluminescence image of the ZnO/ZnTe core-shell

nanowires. (b) Three-dimensional photoluminescence image of the

nanowires were detected at around 2.3 eV when the image is tilted at 45°

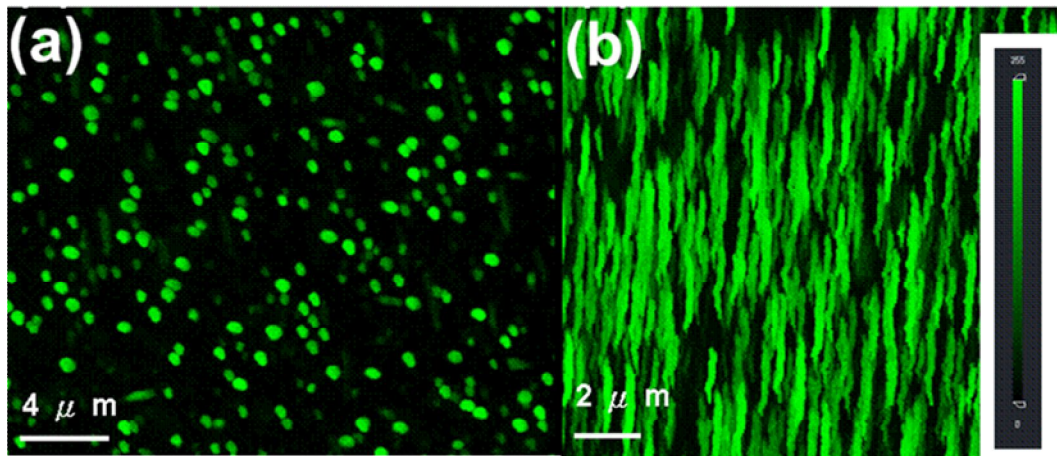and the inset is the scale bar of the PL emission intensity.

the SEM image of the nanowire FET. We can find from this figure that the distance

between the source and drain electrodes was about 0.5 μm for this device.

Figure 5.3.5(c) shows typical current versus source–drain voltage ($I_{ds} - V_{ds}$) curves

at different gate voltages (V_g), obtained from the single ZnO/ZnTe core-shell

nanowire. It can be observed clearly that the source–drain current increases with

increasing negative gate voltage and the device can be turned off completely at

positive gate voltage. It's worth noting that the $I-V$ curves are robust and

reproducible, chemisorption of ambient gas does not appear to have any effect on the

performance of the FET. From the $I-V$ curves we can conclude that the main

transport channel in the ZnO/ZnTe core-shell NW is made of p-type material and thus

the electrical conduction can be attributed to the hole-conduction in the ZnTe shell. It

is known that as-grown ZnO is usually weakly n-type behavior, and the as-grown

ZnTe usually exhibits a p-type behavior [15, 16]. The reason for p-type behavior of

the ZnTe is usually attributed to the Zn vacancies [17] in as-grown ZnTe layer. In

addition, ZnTe nanobelts were also shown to exhibit p-type characteristics [18]. The

measured resistance of the ZnO/ZnTe core-shell nanowire is about $2.9 \times 10^6 \, \Omega$ and the

resistivity (ρ) of the ZnTe shell can be calculated to be about 11.1 Ω cm, which is one

order of magnitude lower than that of ZnTe nanowires (~369.1 Ω cm) [19]. Figure

5.3.5(d) shows source–drain current (I_{ds}) versus gate voltage (V_g) taken at
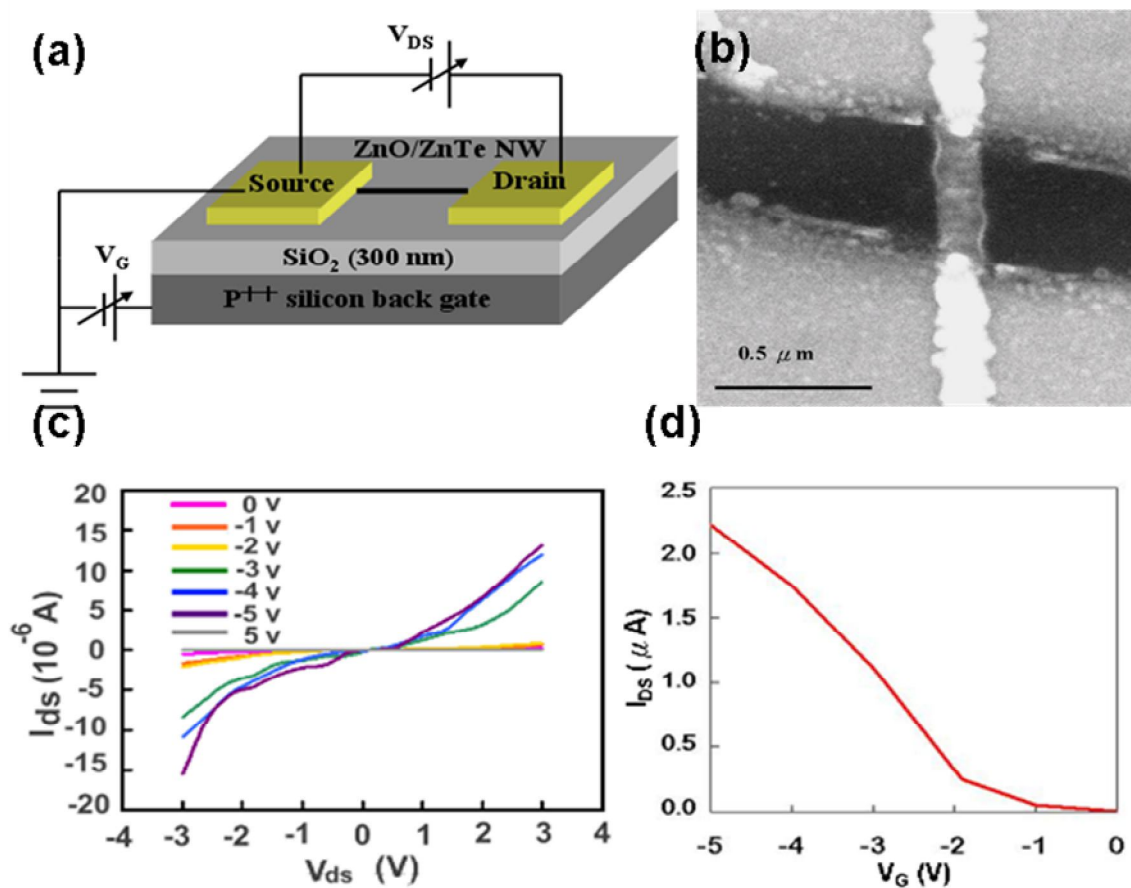
Fig. 5.3.5 (a) Schematic diagram of the single-nanowire FET. (b) SEM image of the

single ZnO/ZnTe core-shell nanowire FET, the distance between the source

and drain electrodes is about 0.5 μm. (c) Current versus source–drain

voltage ($I_{ds} - V_{ds}$) curves at different gate voltages (V_g), obtained from the

single ZnO/ZnTe nanowire FET. (d) Source–drain current (I_{ds}) versus gate

voltage (V_g) taken at source-drain voltage $V_{ds} = 1$ V.

source-drainc voltage $V_{ds} = 1$ V. From the figure we found that the threshold gate voltage V_{th} is around -1.65 V. The transconductance $g_m = dI_{ds}/dV_g$ can be estimated to 3.4×10^{-7} A/V at $V_{ds} = 1$V. Furthermore, the channel mobility of the device can be estimated to be about 13.3 cm^2/V s with the equation $\mu_h = g_m(L^2/CV_{ds})$, where C is the capacitance of the nanowire and the L is the channel length of the nanowire FET. Here, C is given by $C = 2\pi\varepsilon\varepsilon_0 L/\cos h^{-1}(1+h/r)$, where ε is the relative dielectric constant of SiO$_2$=3.9, h is the thickness of the silicon oxide layer (h=300 nm), and r is the nanowire radius (r=150 nm). The mobility is one order of magnitude higher than that of as-grown ZnTe nanowires [15]. The result indicates that low dimensional shell could have higher mobility than that of solid wires, which is consistent with that was reported by Z.H. Chen et al. [20].These results indicate that a FET with good properties could be made from the core-shell nanowires.

5.4 Conclusion

In conclusion, Raman scattering and the photoluminescence measured by laser scanning confocal microscope confirm that the core-shell nanowires have good crystalline quality and good optical properties. Transmission measurement show that the core-shell nanowire could absorb light with energy well below the band gap energy of ZnO and the nanowire arrays appears to have good light trapping ability.

Furthermore, the single core-shell nanowire field effect transistor was successfully fabricated. Electrical measurements of the p-type ZnO/ZnTe FET device reveal that the turn on voltage for the device is about -1.65 V and the hole mobility is 13.3 cm^2/V s, which is one order larger than that of ZnTe. These results indicate the core-shell structure could have potential for applications in optoelectric devices.

References

[1] M. H. Huang, Y. Wu, H. Feick, N. Tran, E. Weber, and P. D. Yang, Adv. Mater. **13**, 113 (2001).

[2] M. J. Zheng, L. D. Zhang, G. H. Li, and W. Z. Shen, Chemical Physics Letters. **363**, 123 (2002).

[3] J. Q. Hu, Q. Li, N. B. Wong, C. S. Lee, and S. T. Lee, Chem. Mater. **14**, 1216 (2002).

[4] E. Ohshima, H. Ogino, I. Niikura, K. Maeda, M. Sato, M. Ito, and T. Fukuda, J. Cryst. Growth **260**, 166 (2004).

[5] H. C. Hsu, H. M. Cheng, C. Y. Wu, H. S. Huang, Y. C. Lee, and W. F. Hsieh, Nanotechnology **17**, 1404 (2006).

[6] Y. W. Wang, L. D. Zhang, G. Z. Wang, X. S. Peng, Z. Q. Chu, and C. H. Liang, J. Cryst. Growth **234**, 171 (2002).

[7] P. X. Gao, Y. Ding, and Z. L. Wang, Nano. Lett. **3**, 1315 (2003).

[8] A. P. Jephcoat, R. J. Hemley, H. K. Mao, R. E. Cohen and M. J. Mehl, Phys. Rev. B. **37**, 4727 (1988).

[9] J. M. Calleja and M. Cardona, Phys. Rev. B. **16**, 3753 (1977).

[10] S. Bhattacharyya, D. Zitoun, Y. Estrin, O. Moshe, D. H. Rich and A. Gedanken, Chem. Mater. **21**, 326 (2009).

[11] Y. Kume, Q. Guo, T. Tanaka, M. Nishio, H. Ogawa and W. Shen, Journal of Crystal Growth. **298**, 441 (2007).

[12] F. Iida, K. Kumazaki, I. Tsubono, N. Kimura, K. Suzuki and K. Imai, Phys. Stat. Sol. (b). **183**, K75 (1994).

[13] F. Iida, N. Takojima, K. Imai and K. Kumazaki, Phys. Stat. Sol. (a). **139**, 531 (1993).

[14] J. Schrier, D. O. Demchenko and L. W. Wang, Nano Lett. **7**, 2377 (2007).

[15] K. Sato, T. Asahi, M. Hanafusa, A. Noda, A. Arakawa, M. Uchida, O. Oda, Y. Yamada, and T. Taguchi, Phys. Status Solidi (a) **180**, 267 (2000).

[16] V. S. John, T. Mahalingam, and J. P. Chu, Solid-State Electron. **49**, 3 (2005).

[17] H. B. Huo, L. Dai, C. Liu, L. P. You, W. Q. Yang, R. M. Ma, G. Z. Ran, and G. G. Qin, Nanotechnology **17**, 5912 (2006).

[18] J. Zhang, P.-C. Chen, G. Shen, J. He, A. Kumbhar, C. Zhou, and J. Fang, Angew. Chem. Int. Ed. **47**, 9469 (2008).

[19] Q. F. Meng, C. B. Jiang, and S. X. Mao, Appl. Phys. Lett. **94**, 043111 (2009).

[20] Z.H. Chen, H. Tang, X. Fan, J.S. Jie, C.S. Lee, S.T. Lee, J. Cryst. Growth **310**, 165 (2008).

Chapter 6

Growth and characterizations of the ZnO/ZnSe core-shell nanowires

6.1 Introduction

In this chapter, we report our studies on the growth and optical characterizations of the aligned ZnO/ZnSe core-shell nanowires. Chemical vapor deposition (CVD) and metal-organic chemical vapor deposition (MOCVD) were used to grow ZnO core and ZnSe shell, and our results show that the ZnO/ZnSe core-shell structures are of good crystalline quality and optical properties.
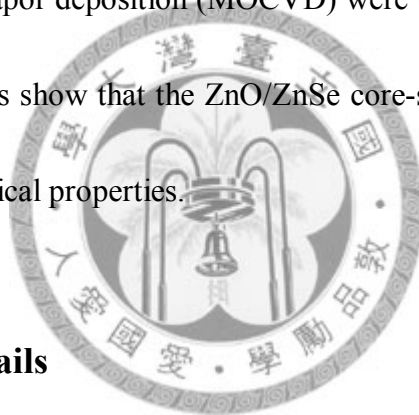
6.2 Experimental details

The vapor–liquid–solid (VLS) [1, 2] and the vapor–solid (VS) [3, 4] methods and other mechanisms for the growth of 1D ZnO nanostructures are well recognized, and these methods have been used to synthesize various compound semiconductor nanostructures. The process of growing ZnO core and ZnSe shell has been described in section 3.3.

The morphology and size distribution of the ZnO/ZnSe core-shell nanowire arrays were studied by scanning electron microscopy (SEM) and crystal structure was

examined by x-ray diffraction (XRD). Raman spectroscopy, transmission and laser scanning confocal microscope were used to study the optical properties of the ZnO/ZnSe core-shell nanowires. For the UV resonant Raman scattering, the sample were excited by the 325 nm line of a He-Cd laser at room temperature.

6.3 Results and discussion

The morphologies of the ZnO nanowires and ZnO/ZnSe core-shell nanowires obtained by SEM are shown in figure 6.3.1. Figure 6.3.1(a) shows vertical ZnO nanowire arrays with length of 7-14 μm and diameter of 100-180 nm, and the inset is the enlargement of one of the ZnO nanowire. Figure 6.3.1(b) is the SEM image of the ZnO/ZnSe core-shell nanowires. Comparing figure 6.3.1(a) with figure 6.3.1(b), we can find that the surface of ZnO nanowires become rough and thick after depositing ZnSe layer, and the diameter of the nanowire increase from 100-180 nm to 150-350 nm, which indicates that ZnSe shell was successfully grown on the surface of ZnO nanowires. The inset in figure 6.3.1(b) is an enlargement of one of ZnO/ZnSe core-shell nanowires. From these figures we can find that the ZnSe shell is smoother than ZnTe shell because the lattice mismatch between ZnSe and ZnO (~8.8 %) is smaller than the lattice mismatch between ZnTe and ZnO (~17 %).

Figure 6.3.2 shows the measured X-ray diffraction patterns of ZnO nanowires and

ZnO/ZnSe core-shell nanowires. The diffraction peak in figure 6.3.2(a) corresponds to the (002) plane of ZnO with wurtzite structure (wurtzite ZnO: a = 0.325 nm and c = 0.521 nm) (JCPDS No 36-1451) and it also demonstrates that the ZnO nanowires are preferentially grown in the c-axis direction. In figure 6.3.2(b), the diffraction peak at $2\theta=27.2°$ corresponds to the (111) plane of ZnSe with zinc-blende structure (zinc-blende ZnSe: a = 0.567 nm) (JCPDS No 80-0021). It is known that ZnSe can crystallize in zinc-blende and wurtzite structures. For bulk ZnSe, the zinc-blende structure transforms to the wurtzite structure when the temperature is above the transition temperature of 1411 ℃. However, decreasing the particle size reduces the transition temperature [5].In our synthesis, the growth temperature of ZnSe is at 530 ℃and at a pressure of 760 torr. Therefore, zinc-blende ZnSe crystal is obtained. We can find in the XRD pattern of ZnO/ZnSe core-shell structure that the peak position of the ZnSe diffraction peak is the same as the diffraction peak of bulk ZnSe , which indicates that the ZnSe layer is fully relaxed due to the large lattice mismatch (~ 8.8 ％) [6] between ZnO (c = 0.521 nm) and ZnSe (a = 0.567 nm), and that ZnO and ZnSe have different crystal structures.

It is well-known that Raman scattering are sensitivity to crystallization, structural disorder and defects in nanostructures. Hexagonal wurtzite ZnO belongs to the C_{6V}^4 (*P63mc*) symmetry group [7]. At the Γ point of the Brillouin zone, the group
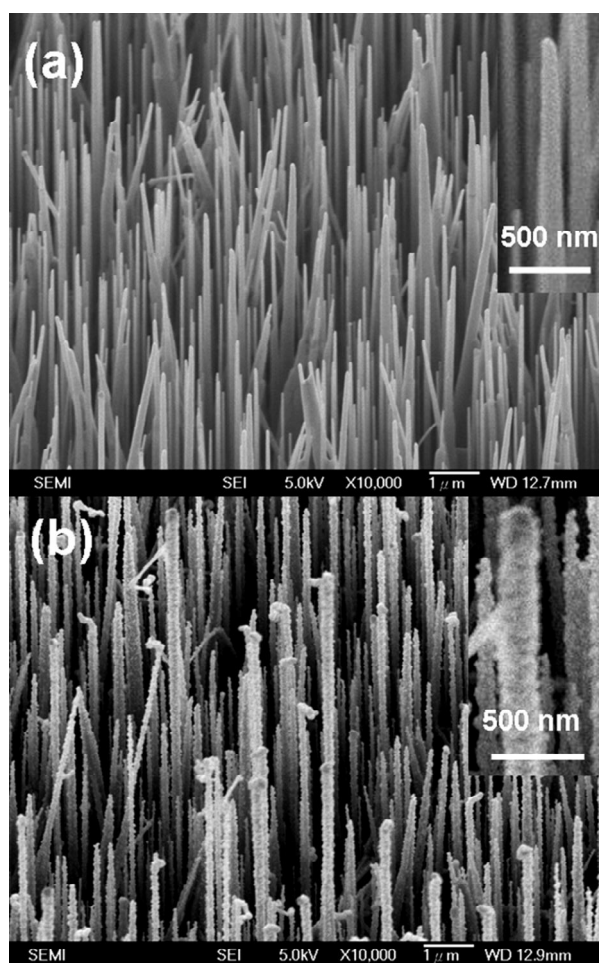
Fig. 6.3.1 (a) and (b) SEM images of ZnO nanowire arrays and ZnO/ZnSe

core-shell nanowire arrays. The insets in (a) and (b) are the enlargements

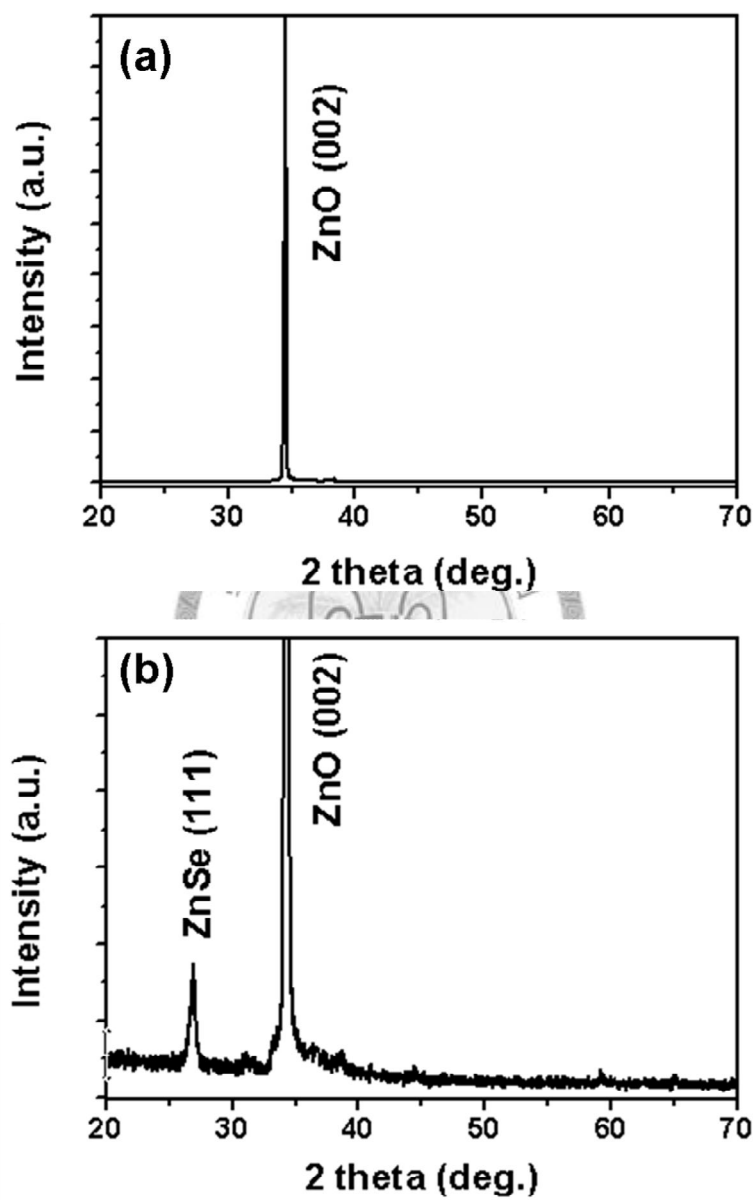of ZnO nanowires and ZnO/ZnSe core-shell nanowires, respectively.

Fig. 6.3.2 X-ray diffraction patterns of (a) ZnO nanowire arrays and (b) ZnO/ZnSe

core-shell nanowire arrays.

theory predicts the existence of the following optic modes：$\Gamma opt = A_1+2B_1+E_1+2E_2$.

These two B_1 modes, B_1 (low) and B_1 (high), are normally silent, and A_1, E_1, and E_2

modes are Raman active. The displacement vectors of the phonon normal modes

reported by F. Decremps *et al*. [8] are illustrated in figure 6.3.3. Room-temperature

Raman spectra of ZnO nanowires and ZnO/ZnSe core-shell nanowires are shown in

figure 6.3.4. In figure 6.3.4, for ZnO nanowire (black line in the figure), the phonon

frequency at 576 cm^{-1} is the A_1 (LO) mode of ZnO, and the phonon with frequency at

1152 cm^{-1} is 2LO mode of ZnO. The E_1 (LO) mode at 584 cm^{-1} is not observed

because the ZnO nanowires are orienting along c-axis. After depositing the ZnSe shell

on ZnO surface to form core-shell structure, the intensity of A_1 (LO) mode of ZnO

decreases because incident light is scattered partly by ZnSe shell (red line in figure

6.3.4). But we can find that for the ZnO/ZnSe core-shell structures, a new peak

appears at 252 cm^{-1}, which can be attributed to the emission of ZnSe LO phonon. As

the LO phonon energy of the ZnSe phonon in the ZnO/ZnSe core-shell nanowires is

the same as that of bulk ZnSe [9, 10], the result indicates that the strain in ZnO/ZnSe

interface is relaxed by misfit dislocation [10]. The results of the optical transmission

measurement on the ZnO nanowires and ZnO/ZnSe core-shell nanowires are shown in

figure 6.3.5. For the sample consists of only ZnO nanowires we could see that it is

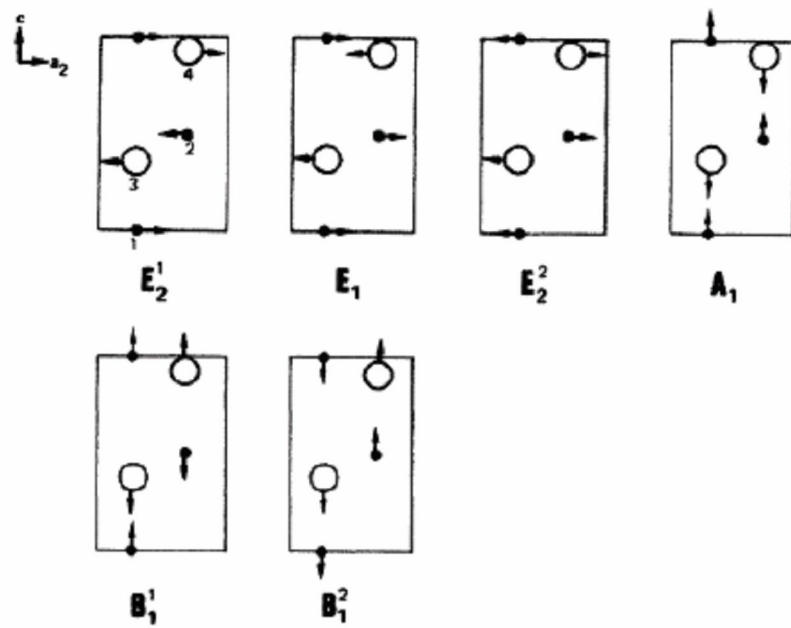transparent in the visible range and strong increase of light absorption occurs
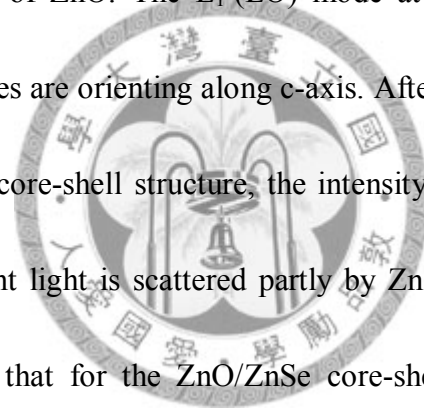
Fig 6.3.3 Displacement vectors for Raman modes of the wurtzite structure. (F.

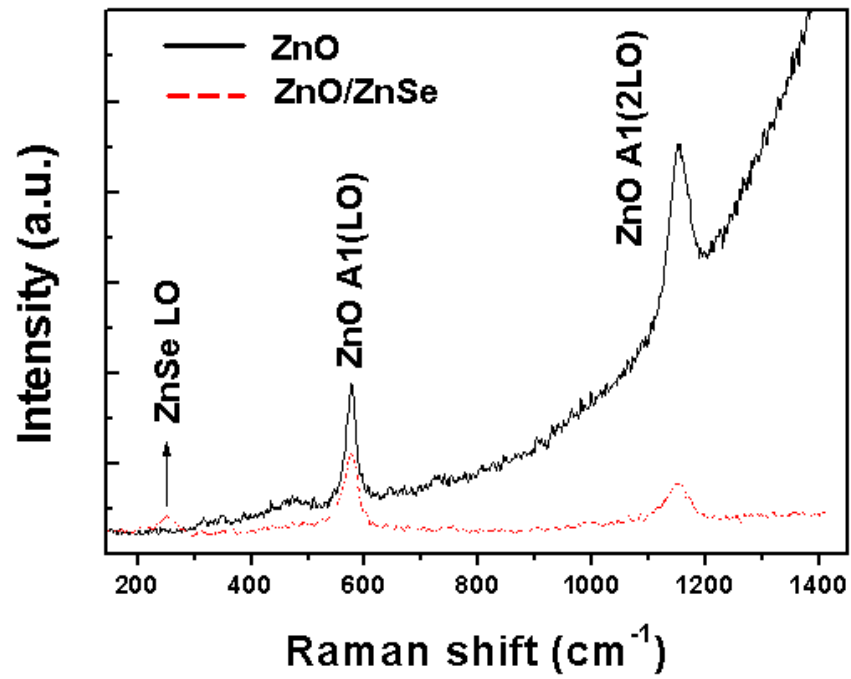Decremps *et al.* , Phys. Rev. B **65**, 092101 (2002))

Fig. 6.3.4 Raman spectra excited at 325 nm of ZnO nanowires (solid line) in

comparison with that of ZnO/ZnSe core-shell nanowires (dashed line).

near and above the energy gap of ZnO, it indicate that ZnO is only suitable for UV light absorption. But for the ZnO/ZnSe nanowires, the transmission curve is clearly different from that of the ZnO nanowires. We can find that the visible light absorption of ZnO/ZnSe core-shell nanowires is stronger than that of ZnO nanowires. In addition, there are two drops in the transmission curves of ZnO/ZnSe nanowires, one is near 380 nm and the other is near 500 nm, corresponding to the bandgap energy of ZnO and the defect emission energy of ZnSe. The results show the ZnO/ZnSe core-shell nanowires structure has good light-trapping effect due to multiple reflections and has better light absorption because it has a ZnSe shell. Comparing ZnO/ZnSe core-shell nanowires with ZnO/ZnTe core-shell nanowires, we can find that the visible light absorption of ZnO/ZnSe core-shell nanowires is smaller than of ZnO/ZnTe core-shell nanowires. This is because the absorption coefficient of ZnSe ($\sim 2\times10^4$ cm^{-1}) [11] is smaller than that of ZnTe ($\sim 4.5\times10^4$ cm^{-1}) [12] and the ZnSe layer is thinner than ZnTe layer.

Laser scanning confocal microscope is a useful technique to study optical properties of different planes in z-axis (vertical to the substrate) and 3D-luminescence intensity in nanostructures. Figure 6.3.5(a) and figure 6.3.5(b) are the top view and 45°-view of the luminescence image of the ZnO/ZnSe core-shell nanowires. From figure 6.3.5(a) we can find that the distribution of nanowires is uniform around the
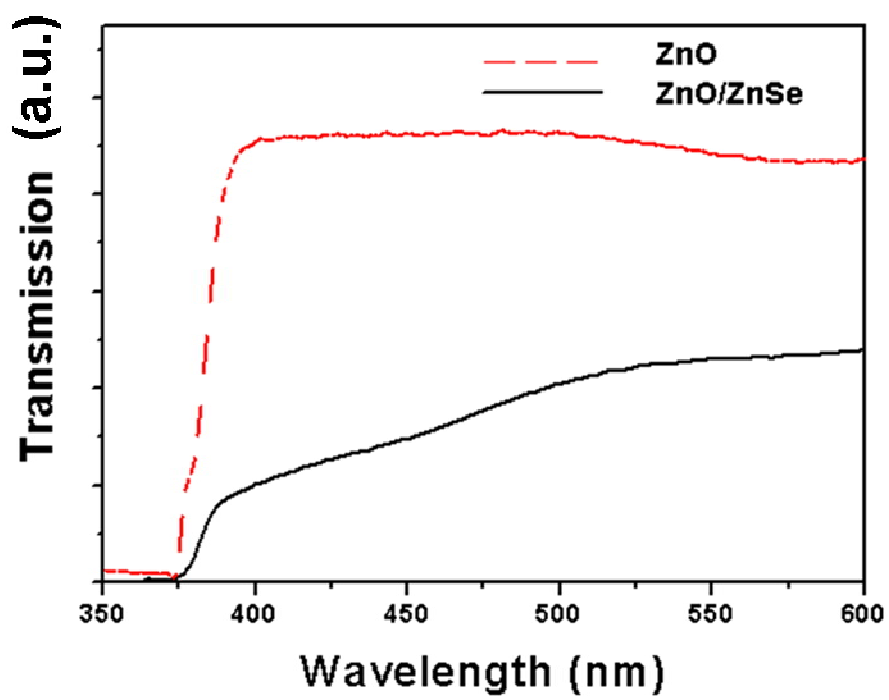
Fig. 6.3.5 Transmission spectra of ZnO nanowires (dashed line) and ZnO/ZnSe

core-shell nanowires (solid line).

sample and the density of nanowires is high. The 3D-luminescence image is shown in

figure 6.3.6(b). From this image we can see that the intensity of bandgap emission of

the ZnSe is uniform along the z-axis and the light emission properties of the ZnSe

shell grown on the ZnO core is also quite similar. Room-temperature PL spectrum of

ZnO/ZnSe core-shell nanowires is shown in figure 6.3.6(c). The spectrum consists of

three Gaussian curves with the peak energies corresponding to 2.84 eV, 2.72 eV and

2.56 eV, respectively. The peak energy at 2.84 eV could be attributed to the defect

emission of ZnO core. The peak energy at 2.72 eV is attributed to bandgap emission

of ZnSe shell, and the weak emission around at 2.56 eV is called the Y line emission,

which is the result from the structure defects of the ZnSe crystal such as dislocations

[13, 14]. These results show that the ZnO/ZnSe core-shell nanowires have good

optical properties.
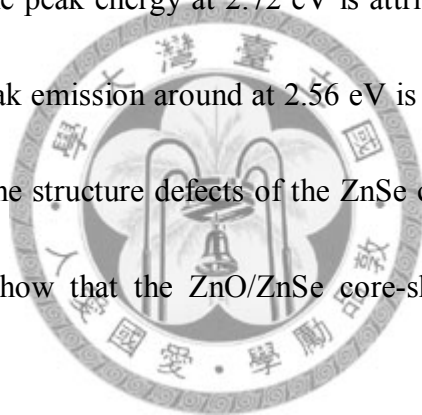
6.4 Conclusion

We have successfully synthesized ZnO/ZnSe core-shell nanowires by using CVD

and MOCVD. Detailed structural studies showed that the core-shell nanowires are

composed of ZnO core with hexagonal wurtzite structure and ZnSe shell with

znic-blende structure. From transmission measurement we can find that the vertically

aligned ZnO/ZnSe core-shell nanowire arrays have a good light-trapping effect. In the
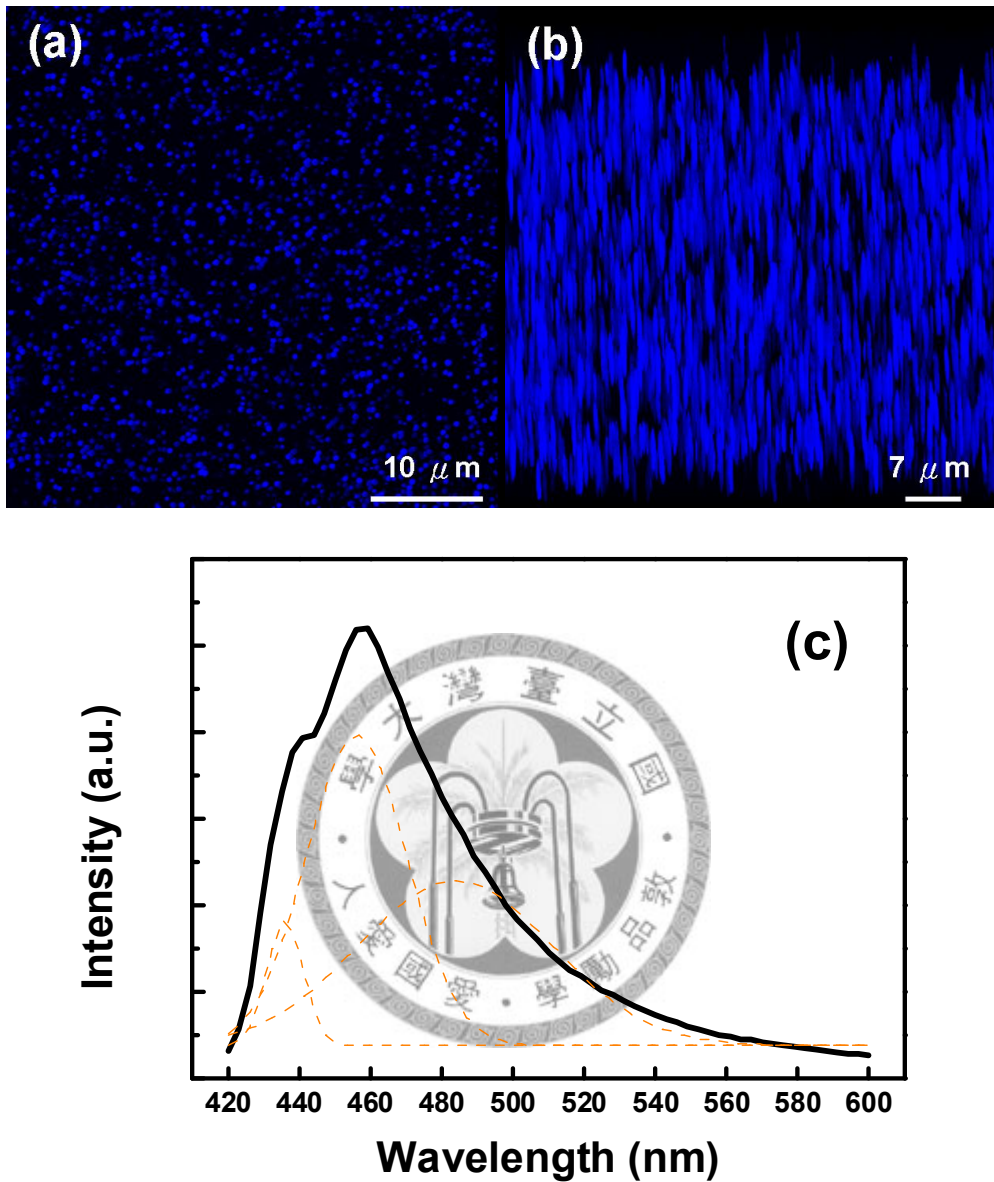
Fig. 6.3.6 (a) Top view of the photoluminescence image of the ZnO/ZnSe

core-shell nanowires. (b) is the three-dimensional photoluminescence image

of the core-shell nanowires when the image is tilted at 45°. (c) PL spectrum

of the ZnO/ZnSe nanowires was measured at room temperature under

excitation by the 405 nm line of a diode laser.

PL spectrum the defect emission and bandgap emission from ZnSe layer were observed. From the XRD pattern and the Raman spectrum, we can find that the strain between the ZnO and ZnSe layer is relaxed by misfit dislocation. This work showed that the ZnO/ZnSe core-shell nanowirs have good optical and structural properties and have potential in making photovoltaic cell and optoelectronic devices.

References

[1] M. H. Huang, Y. Wu, H. Feick, N. Tran, E. Weber, and P. D. Yang, Adv. Mater. **13**, 113 (2001).

[2] M. H. Huang, S. Mao, H. Feick, H. Yun, Y. Wu, H. Kind, E. Weber, R. Russo, and P. D. Yang, Science **292**, 1897 (2001).

[3] Z. W. Pan, Z. R. Dai, and Z. L. Wang, Science, **291**, 1947 (2001).

[4] J. Q. Hu, Q. Li, N. B. Wong, C. S. Lee, and S. T. Lee, Chem. Mater. **14**, 1216 (2002).

[5] S. B. Qadri, E. F. Skelton, D. Hsu, A. D. Dinsmore, J. Yang, H. F. Gray, and B. R. Ratna, Phys. Rev. B **60**, 9191 (1999).

[6] K. Wang, J. Chen, W. Zhou, Y. Zhang, Y. Yan, J. Pern, and A. Mascarenhas, Adv. Mater. **20**, 3248 (2008).

[7] A. P. Jephcoat, R. J. Hemley, H. K. Mao, R. E. Cohen, and M. J. Mehl, Phys. Rev. B **37**, 4727 (1988).

[8] F. Decremps, J. Pellicer-Porres, A.M. Saitta, J. C. Chervin, and A. Polian, Phys. Rev. B **65**, 092101 (2002).

[9] M. Y. Valakh, S. V. Ivanov, N. Mestres, J. Pascual, T. V. Shubina, S. V. Sorokin, V. V. Streltchuk, G. Pozinaand, and B. Monemar, Semicond. Sci. Technol. **17**, 173 (2002).

[10] T. Matsumoto, T. Kato, M. Hosoki, and T. Ishida, Jap. J. Appl. Phys. **26**, L576 (1987).

[11] S. Adachi, and T. Taguchi, Phys. Rev B **43**, 9569 (1991).

[12] B. Langen, H. Leiderer, W. Limmer, W. Gebhardt, M. Ruff, and U. Rössler, J. Cryst. Growth **101**, 718 (1990).

[13] K. Maehashi, N. Morota, Y. Murase, and H. Nakashima, J. Appl. Phys. **38**, 1339 (1999).
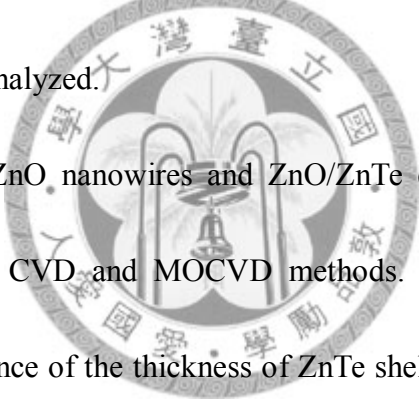
[14] P. J. Dean, Phys. Stat. Sol. (a) **81**, 625 (1984).

Chapter 7

Conclusions

In this thesis, we have presented some novel methods of growing nanowires and core-shell nanowires structure of II-VI semiconductor. In addition, their morphology, structure and optical properties have been confirmed by scanning electron microscopy (SEM), X-ray diffraction (XRD), transmission electron microscope (TEM), Raman scattering, laser scanning confocal microscope (LSCM), and field effect transistor have been measured and analyzed.

In chapter 4, vertical ZnO nanowires and ZnO/ZnTe core-shell nanowires have been fabricated by using CVD and MOCVD methods. The TEM images can be observed that the dependence of the thickness of ZnTe shell grown on ZnO nanowire surface and the deposited time of ZnTe is about linear. The crystal structures were confirmed by XRD patterns and HRTEM, these results showed that the ZnO nanowire has the (002) plane of wurtzite structure and the ZnTe shell has the (111) plane of znic-blende structure. In chapter 5, the ZnO/ZnTe core-shell nanowires with 5-10 μm long have been fabricated and the single ZnO/ZnTe core-shell nanowire FET was measured. In the Raman spectrum, the A_1 (LO) mode of ZnO nanowires and the LO mode of ZnTe shell can be observed. The transmission curves showed that the visible

light absorption increased strongly after coating with ZnTe layer on the ZnO nanowires surface. The Electrical measurements showed that the turn on voltage of the p-type ZnO/ZnTe FET device is about -1.65 V, and the hole mobility of the FET is about 13.3 cm^2 /V s, which is one order of magnitude larger than that of solid wire. In chapter 6, we have successfully synthesized the ZnO nanowires and the ZnO/ZnSe core-shell nanowires by using CVD and MOCVD. The structural studies showed that the core-shell nanowires are composed of ZnO core with wurtzite structure and ZnSe shell with znic-blende structure. XRD patterns and Raman scattering showed the strains in the ZnSe layer are relaxed by misfit dislocation. Both band edge emission and defect emission from ZnSe layer can be observed in PL spectrum. From the confocal scanning PL measurement we find that the emission intensity along the nanorod is quite uniform.